An improved global land cover mapping in 2015 with 30 m resolution (GLC-2015) based on a multi-source product fusion approach

Bingjie Li [1], Xiaocong Xu [1], Xiaoping Liu [1][2], Qian Shi [1], Haoming Zhuang [1], Yaotong Cai [1] and Da He [1]

[1]School of Geography and Planning, Sun Yat-Sen University, Guangzhou, 510275, China

[2]Southern Marine Science and Engineering Guangdong Laboratory (Zhuhai), Zhuhai, 519080, China

Correspondence to: Xiaoping Liu (liuxp3@mail.sysu.edu.cn)

Abstract. Global land cover (GLC) information with fine spatial resolution is a fundamental data input for studies on biogeochemical cycles of the Earth system and global climate change. Although there are several public GLC products with 30 m resolution, considerable inconsistencies were found among them especially in fragmented regions and transition zones, which brings great uncertainties to various application tasks. In this paper, we developed an improved global land cover map in 2015 with 30 m resolution (GLC-2015) by fusing multiple existing land cover (LC) products based on the Dempster-Shafer theory of evidence (DSET). Firstly, we used more than 160,000 global point-based samples to locally evaluated the reliability of the input GLC products for each land cover class within each 4°×4° geographical grid for the establishment of the basic probability assignment (BPA) function. Then, the Dempster's rule of combination was used for each 30 m pixel to derive the combined probability mass of each possible land cover class from all the candidate maps. Finally, each pixel was determined with a land cover class based on a decision rule. Through this fusing process, each pixel is expected to be assigned with the land cover class that contributes to achieve a higher accuracy. We assessed our product separately with 34,711 global point-based samples and 201 global patch-based samples. Results show that, the GLC-2015 map achieved the highest mapping performance globally, continentally, and eco-regionally compared with the existing 30 m GLC maps, with an overall accuracy of 79.5% (83.6%) and a kappa coefficient of 0.757 (0.566) against the point-based (patch-based) validation samples. Additionally, we found that the GLC-2015 map showed substantial outperformance in the areas of

inconsistency, with an accuracy improvement of 19.3%-28.0% in areas of moderate inconsistency, and

27.5%-29.7% in areas of high inconsistency. Hopefully, this improved GLC-2015 product can be applied

to reduce uncertainties in the research on global environmental changes, ecosystem service assessments,

and hazard damage evaluations, etc. The GLC-2015 map developed in this study is available at

https://doi.org/10.6084/m9.figshare.22358143.v2 (Li et al., 2022).

1. Introduction

Land cover (LC), influenced by both nature and human activities (Running, 2008; Gong et al., 2013;

Song et al., 2018; Liu et al., 2021a), is a significant component of the Earth system (Yang and Huang,

2021). Global land cover (GLC) products can serve as fundamental data for various studies, such as

climate and environmental changes (Bounoua et al., 2002; Foley et al., 2005; Grimm et al., 2008; Yang

et al., 2013; Schewe et al., 2019), food security (Verburg et al., 2013; Ban et al., 2015), carbon cycling

(Moody and Woodcock, 1994; Defries et al., 2002; Gómez et al., 2016), biodiversity conservation

(Chapin et al., 2000; Giri et al., 2005) and land management (Mayaux et al., 2004; Verburg et al., 2011).

Therefore, there is a pressing need for detailed, accurate, and high-quality GLC product to support global

change research and sustainable development.

In the preliminary stage, LC mapping mainly relied on visual interpretation, which is time-

consuming, labor-intensive and difficult to be applied at the global scale (Gong, 2012). In recent decades,

satellite remote sensing data, which can provide information of large area coverage and long-term

monitoring, has been adopted to generate GLC products. With coarse resolution satellite data such as

Advanced Very High Resolution Radiometer (AVHRR), Moderate Resolution Imaging

Spectroradiometer (MODIS), Medium Resolution Imaging Spectrometer (MERIS), and Global Land

Surface Satellite (GLASS), a variety of GLC products have been developed at 5 km to 300 m

resolution(Loveland et al., 2000; Hansen et al., 2000; Bartholomé and Belward, 2005; Friedl et al., 2010;

Defourny et al., 2018; Liu et al., 2020a). Although these GLC products have been widely applied to many

applications, it has been proved that the differences between sensors, classification systems, and

considerably low accuracies in areas prevent harmonization of these products (Herold et al., 2008;

Verburg et al., 2011; Grekousis et al., 2015). Also, these products are far from providing enough fine

spatial details of LC due to their relatively coarse spatial resolution, which does not meet the demand of

55   many studies (Giri et al., 2013; Yang et al., 2017). To allow researches which can capture most human

56   activity, finer-resolution (e.g., 30 m) GLC products are demanded (Giri et al., 2013).

57   With the free accessibility of high-resolution satellite remote sensing data, GLC mapping at fine

58   resolution has been successfully conducted. Using Landsat imagery, there has been a milestone

59   achievement that the two GLC products are generated with fine resolution of 30 m, namely Finer

60   Resolution Observation and Monitoring of Global Land Cover product (FROM_GLC)(Gong et al., 2013)

61   and Globeland30 (Chen et al., 2015). After that, a 30 m-resolution GLC mapping in 2017 was achieved

62   using the first all-season sample set (Li et al., 2017). More recently, Zhang et al. (2021) used both Landsat

63   time series imagery and high-quality training data from the Global Spatial Temporal Spectra Library

64   (GSPECLib) to produce a 30 m GLC map in 2015 (GLC_FCS30) with a two-level classification scheme.

65   Several attempts have been made to improve accuracy of 30 m GLC products which are prevail in the

66   generation of GLC mapping task over the last few years. FROM_GLC was created by employing four

67   classification algorithms to classify the Landsat images and choosing time series of MODIS EVI data for

68   training and test. Globeland30 was created by proposing a pixel-object-knowledge-based (POK) method

69   to assure consistency and accuracy. GLC_FCS30 was generated by adopting local adaptive random forest

70   models with high-quality training samples derived from GSPECLib. The Globeland30, FROM_GLC,

71   and GLC_FCS30 are excellent and indispensable GLC products which have contributed much to various

72   researches, such as biodiversity conservation (Wu et al., 2020; Meng et al., 2023), climate change (Kim

73   et al., 2016; Xue et al., 2021; Zheng et al., 2022), and land management (Shafizadeh-Moghadam et al.,

74   2019). In addition to these multiple-class GLC products, GLC products for individual LC classes, such

75   as cropland (Yu et al., 2013; Lu et al., 2020), forest (Hansen et al., 2013; Shimada et al., 2014; Zhang et

76   al., 2020), wetland (Hu et al., 2017; Zhang et al., 2023), water bodies (Liao et al., 2014; Pekel et al., 2016;

77   Pickens et al., 2020), and impervious surfaces (Gong et al., 2020; Huang et al., 2021; Huang et al., 2022;

78   Liu et al., 2020b), have been successfully generated.

79   Despite the great efforts in producing more accurate products, the existing 30 m GLC products still

80   show unstable performance in certain LC classes and some specific areas (Sun et al., 2016; Kang et al.,

81   2020). Furthermore, the existing 30 m products showed great agreement in overall spatial distribution

82   patterns but significant spatial inconsistency in some specific areas (heterogeneous areas and transition

83   zones) and spectrally similar classes (forest and shrubland, cropland and grassland) (Gao et al., 2020;

84   Liu et al., 2021b). The spatial inconsistency between the existing 30m GLC products are resulted from

85   differences in their classification systems, classification techniques employed, source data, and spatial

86   distribution and size of training samples (Yang et al., 2017; Gao et al., 2020). Due to the aforesaid

87   limitations, users of GLC products still have difficulties in an appropriate selection of data for their

88   specific application. Ultimately, this situation leads to uncertainties in outcomes of related researches

89   when different 30 m GLC products are used. For GLC mapping with fine spatial resolution, more efforts

90   should be focused on improving the mapping in heterogenous and fragmented landscape (Herold et al.,

91   2008; Liu et al., 2021b). Therefore, it is pressing to generate a more accurate and reliable GLC product

92   with high classification accuracy, especially for spatially inconsistent regions and low-accuracy LC

93   classes.

94   According to Gong et al. (2016), inconsistencies between LC products indicate available

95   complementary information and more robust and reliable data can be generated by integrating the input

96   maps with the data fusion method. Given that different maps have disagreement and provide accurate

97   information in different locations, we can make a best choice for the class label assigned to each pixel

98   by weighting the credibility of all the available information and combining them through a decision rule

99   (Clinton et al., 2015). In this way, the output map of integration on input maps can reduce the overall risk

100   of assigning a wrong class label to a pixel and at least achieve the average performance of input maps.

101   Several attempts have been made to produce an accurate and consistent LC map using various methods,

102   such as majority voting (MV), fuzzy agreement and Bayesian theory. Iwao et al. (2011) created a GLC

103   map based on a simple majority voting method. Jung et al. (2006) generated a 1km GLC map by

104   combination of MODIS, GLC2000 and GLCC data based on fuzzy agreement scoring. Subsequently,

105   Fritz et al. (2011) extended the synergy method of Jung et al. (2006) by ranking LC maps and mapped

106   the cropland extent in Sub-Saharan Africa. See et al. (2015) generated two GLC products by integrating

107   medium resolution LC products with geographically weighted regression (GWR). Gengler and Bogaert

108   (2018) proposed a Bayesian data fusion method and applied it to the LC mapping for a specific region in

109   Belgium. All these researches have demonstrated that fusion method can create an integrated LC product

110   where the mapping accuracy is greatly improved by combing the best of candidate maps. However, the

111   MV method is sensitive to the quality of the candidate maps and has significant uncertainties when the

112   input products exhibit great disagreement (Chen and Venkataramanan, 2005). The fuzzy agreement is

113 highly subjective since it depends on expert assessment, while the Bayesian theory requires a prior

114 knowledge or conditional probabilities and fails to handle the states of ignorance (Liu and Xu, 2021).

115   The Dempster-Shafer theory of evidence (DSET) is an evidence-based approach to reason with

116 uncertainties. Unlike the majority voting, the DSET method can discount evidence from inaccurate

117 information with a probability mass that reflects the degree of belief rather than a binary decision (Razi

118 et al., 2019). In contrast to the Bayesian theory, the DSET can integrate evidence from a variety of sources

119 without the requirement of prior knowledge (Chen and Venkataramanan, 2005). Moreover, the reliability

120 of the final fused results based on the DSET method is measured with a total degree of belief. Although

121 previous literatures focused on the application of the DSET method in multisource data aggregation, very

122 little research has been conducted at a global scale due to the lack of accurate and sufficient samples and

123 the demand for adequate computing resources.

124   In this research, we propose a multi-source product fusion approach on the Google Earth Engine

125 (GEE) platform to produce an improved GLC product in 2015 (GLC-2015) with 30 m resolution. The

126 fusion approach we proposed aims to deal with the inconsistency between previous 30 m GLC products

127 and generate a map which has better mapping performance than any of the candidate maps by evaluating

128 the mapping accuracy of these existing products at the local scale and choosing the most credible LC

129 class. To fulfill the purpose, we first performed reliability evaluation, where the accuracy of each GLC

130 product for each LC class in each $4° \times 4°$ geographical grid is regarded as the evidential probability to

131 create the basic probability assignment (BPA) function. Then, the BPA values of all the LC classes from

132 different GLC products were fused according to the Dempster's rule of combination. Finally, the GLC-

133 2015 map was integrated after a final accepted LC class with the maximum combined probability mass

134 was assigned to each 30 m pixel. The GLC-2015 map was separately validated with two different

135 validation sets, namely global point-based samples and global patch-based samples, and compared with

136 three existing multiple-class GLC products. Moreover, we provided an analysis for the mapping

137 improvement of the GLC-2015 compared to other products in areas of high mapping inconsistency. The

138 GLC-2015 map is proved to be accurate and credible and can significantly improve the mapping accuracy

139 in areas of high inconsistency.

140   **2. Datasets**

141   **2.1 Multiple-class GLC products**

142   Three existing 30m GLC products with multiple classes, including GlobeLand30, FROM_GLC and

143   GLC_FCS30, were employed as input maps in the fusion based on DSET. A summary of their detailed

144   information is shown in Table 1.

145   GlobeLand30, a widely-used global geo-information product, was produced by the POK-based

146   method using Landsat and HJ-1 satellite images. Globeland30 products are freely accessible online at

147   the website (http://www.globalland30.org) for 2000 and 2010. From the accuracy assessment, the

148   Globeland30 for the year 2010 had an overall accuracy excessed 80% using large samples (Chen et al.,

149   2015). Although the data time of GlobeLand30 is 2010, which has a five-year gap with other products,

150   it was used because the changed areas of LC caused by the time interval are tiny compared to the global

151   land area. In addition, there is relatively less uncertainty due to LC changes than due to inaccurate

152   classification (Xu et al., 2014). Most spatial disagreements between the existing maps are about

153   classification errors rather than LC changes over the time interval (Mccallum et al., 2006; See et al.,

154   2015).

155   FROM_GLC was first generated using numerous Landsat images, which has a fine classification

156   system with a two-level structure. It achieved an OA of 64.5% through validation with the complete test

157   samples and 71.5% with a subset of test samples in homogeneous areas (Gong et al., 2013). We used the

158   version of 2015 for the fusion.

159   GLC_FCS30 was developed using Landsat time series data and large training samples from the

160   GSPECLib. It has a two-level classification scheme that contains 16 global LCCS LC classes and 14

161   detailed regional LC classes. The overall accuracy of the GLC_FCS30 according to LCCS level-1

162   validation scheme reached 71.4% (Zhang et al., 2021).

163   **Table 1. Detailed information of GLC products and national-scale LC products used in this paper.**

Product name	Satellite sensors	Year of reference	Access	Literature
Globeland30	Landsat TM/ETM+ HJ-1 A/B	2010	http://www.globallandcover.com/	(Chen et al., 2015)
FROM_GLC	Landsat TM/ETM+/OLI	2015	http://data.ess.tsinghua.edu.cn/	(Gong et al., 2013)

GLC_FCS30	Landsat OLI	2015	https://doi.org/10.5281/zenodo.3986872	(Zhang et al., 2021)
GAUD	Landsat TM/ETM+/OLI	2015	https://doi.org/10.6084/m9.figshare.115131 78.v1	(Liu et al., 2020c)
GFC	Landsat TM/ETM+	2015	http://earthenginepartners.appspot.com/scie nce-2013-global-forest	(Hansen et al., 2013)
JRC GSW	Landsat TM/ETM+/OLI	2015	http://global-surface-water.appspot.com/	(Pekel et al., 2016)
GMW	ALOS PALSAR Landsat TM/ETM+	2015	https://data.unep-wcmc.org/datasets/45	(Bunting et al., 2018)
NLCD 2016	Landsat TM /OLI	2016	https://www.mrlc.gov/data/nlcd-2016-land- cover-conus	(Yang et al., 2018)
CLUD	Landsat TM HJ-1 CBERS-1	2015	/	(Liu et al., 2014)
CLCD	Landsat TM/ETM+/OLI	2015	https://doi.org/10.5281/zenodo.4417810	(Yang and Huang, 2021)

2.2 Single-class GLC products

To improve the quality of the fusing result, a set of highly qualified GLC products with single class at 30 m fine resolution were also used. Compared to the multiple-class GLC products, these single-class GLC products are more likely to provide accurate information since they usually focus on promoting mapping performance of specific LC class. These products include Global Forest Change (GFC) (Hansen et al., 2013), Global Annual Urban Dynamics (GAUD) (Liu et al., 2020b), Joint Research Centre's Global Surface Water (JRC GSW) (Pekel et al., 2016), and Global Mangrove Watch (GMW) (Bunting et al., 2018). While these single-class products are either annual or multi-epoch, we only selected these products in the target year of 2015. The background information of these single-class products was considered as another land cover class (e.g., non-water) participating in the fusion. The accuracy of the background information was defaulted to 0 since it did not provide information about any of the other nine categories in our classification system. Table 1 also describes the information of these selected single-class GLC products.

GFC was resulted from a time-series analysis of growing season Landsat scenes, aiming to provide

178   information about global tree cover extent, gain, and loss at a 30m spatial resolution. The accuracy

179   assessment was performed at global and climate domain scales and the forest gain reached an overall

180   accuracy of 99.6% and forest loss reached 99.7% across the globe (Hansen et al., 2013). Up to now, it

181   has a temporary coverage from 2000 to 2020.

182   GAUD, which provides 30m annual urban extent for the time period of 1985 to 2015, was generated

183   using numerous Landsat images with both data fusion approach and temporal segmentation approach on

184   the GEE platform. Validation was conducted across different urban ecoregions and the globe by the

185   product developer. The accuracy of mapping urbanized year was 76% for the period of 1985 to 2000 and

186   82% for the period of 2000 to 2015 at humid regions worldwide (Liu et al., 2020c).

187   JRC GSW dataset provides a monthly presentation of global surface water changes from 1984 to

188   2015 at a fine 30 m resolution. Expert systems, visual analytics and evidential reasoning were exploited

189   to detect water extent and changes. Based on 40,124 validation points over the globe and across the 32

190   years, commission accuracies were determined with overall accuracies of 99.45% (TM), 99.35% (ETM+)

191   and 99.54% (OLI) and omission accuracies were reflected in overall accuracies of 97.01% (TM), 95.79%

192   (ETM+) and 96.25%(OLI) (Pekel et al., 2016). We used the GSW Yearly Water Classification History

193   v1.1 in the GEE catalog. A single 'waterClass' band is present in each image that provides the water's

194   seasonality throughout the year with four types: no data, no water, seasonal water, and permanent water.

195   Since the seasonal water in GSW data is not as reliable as the permanent water (Meyer et al., 2020), we

196   selected permanent water bodies and excluded seasonal water bodies.

197   GMW dataset was produced as a result of the GMW initiative, which aims to provide consistent

198   information of mangrove extent. The global mangrove map in 2010 was generated as a baseline map

199   employing the Extremely Randomized Trees classifier to classify ALOS PALSAR and Landsat imagery.

200   Assessed by a total of 53,878 sample points globally, the overall accuracy of the baseline map reached

201   95.3% and the producer's accuracy achieved 94.0% (Bunting et al., 2018). Based on the baseline in 2010,

202   mangrove extent maps for six epochs between 1996 and 2016 have been established and annual change

203   monitoring from 2018 and onwards are undertaken.

204   **2.3 National-scale LC products**

205   Land cover products which focus on a national scale are more likely to possess higher accuracy

206   because they were produced by experts who have good knowledge of land cover classes nationally. Thus,

207   the National Land Cover Database 2016 (NLCD 2016) for the year 2016 over the conterminous United

208   States (CONUS) (Yang et al., 2018), China's land-use/cover dataset (CLUD) (Liu et al., 2014) for 2015,

209   and the annual China land cover dataset (CLCD) (Yang and Huang, 2021) for 2015 were also included

210   in the fusion. The detailed information of these national-scale products was listed in Table 1.

211   NLCD 2016 database, which provides continuous and accurate information about land cover and

212   change from 2001 to 2016 at an interval of 2 or 3 years, was produced based on a pixel- and object-based

213   approach and an effective post-classification process (Yang et al., 2018). The level-1 and level-2 overall

214   accuracy of NLCD 2016 database for 2016 was 90.6% and 86.4% for CONUS, respectively (Wickham

215   et al., 2021). CLUD, developed by the digital interpretation method using Landsat images, provide land

216   cover information over China from 1980s to 2015. The overall accuracy of CLUD reached 94.3% and

217   91.2% for level-1 and level-2 land cover classes, respectively (Liu et al., 2014). CLCD was generated

218   with stable training samples derived from CLUD and Landsat time series. Assessed with 5463 validation

219   samples, CLCD obtained an overall accuracy of 79.31% (Yang and Huang, 2021).

220   **2.4 Global point-based and patch-based samples**

221   In this study, we collected two sets of global samples, namely the global point-based samples and the

222   global patch-based samples. To collect representative and sufficient samples efficiently, we divided the

223   world's terrestrial area into 4° × 4° geographical grids. A total of 1,507 grids are distributed evenly across

224   the globe, shown as Figure 1.
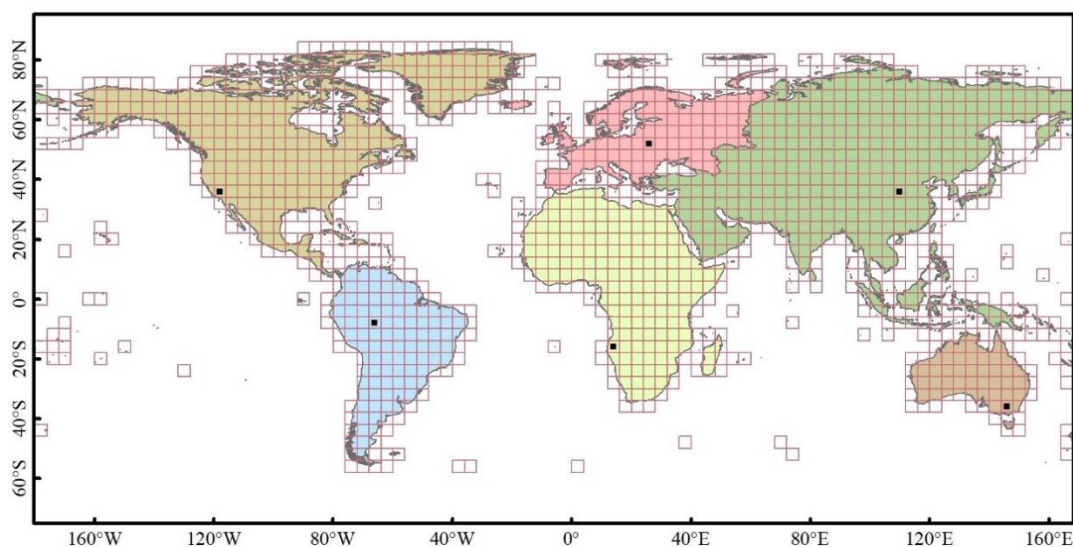
225

226   **Figure 1. Spatial distribution of the 4° × 4° geographical grids over the world. Six black rectangle tiles with**

227   **size of 0.25° were used for visual comparation between our product and other three products.**

228   To derive the global point-based samples, we adopted stratified random sampling in each grid. The

229   stratified random sampling depends on area ratio of LC classes from a LC product. We used the

230   FROM_GLC as prior knowledge rather than the Globeland30 and GLC_FCS30 with two considerations:

231   (1) the FROM_GLC has the same data time as our target map (GLC-2015) while the Globeland30 has a

232   5-year interval from our samples, which affects the size of samples for each LC class; (2)the 10 level-1

233   land cover classes of the FROM_GLC is similar to that in the classification system of the GLC-2015,

234   while the GLC_FCS30 has differences with the GLC-2015 in the classification scheme and definition of

235   land cover classes. First, the FROM_GLC product was used to calculate the area ratio of each LC class.

236   Then, points were randomly extracted from the FROM_GLC according to the area ratio and spatial

237   location of each class. Finally, more than 200,000 global samples were collected. Through the sampling

238   method mentioned above, the global point-based samples were even across the globe and sufficient for

239   each LC class in each grid. Therefore, more than 50 points could be easily derived for LC classes with a

240   small area ratio in the $4° \times 4°$ grid. The FROM_GLC shows low accuracy for some LC classes, especially

241   for cropland and forest (Gao et al., 2020; Liu et al., 2021b; Zhang et al., 2021; Zhang et al., 2022). If the

242   global samples were extracted with LC class label from the FROM_GLC, there would be inevitable

243   errors. Therefore, the FROM_GLC was only used to determine the size and location of samples for each

244   LC class. Instead, all the points were manually labeled according to Google Earth high-resolution images.

245   The whole sample set was randomly split into two subsets: 80% of the global samples were used to assess

246   the accuracy of each GLC product for various LC classes at the global scale and in each grid. The

247   remaining 20% were used for the validation of the GLC-2015 map and data inter-comparison between

248   different GLC products. Figure 2 presents the distribution of the whole global point-based samples and

249   the subset for accuracy assessment and data inter-comparison.
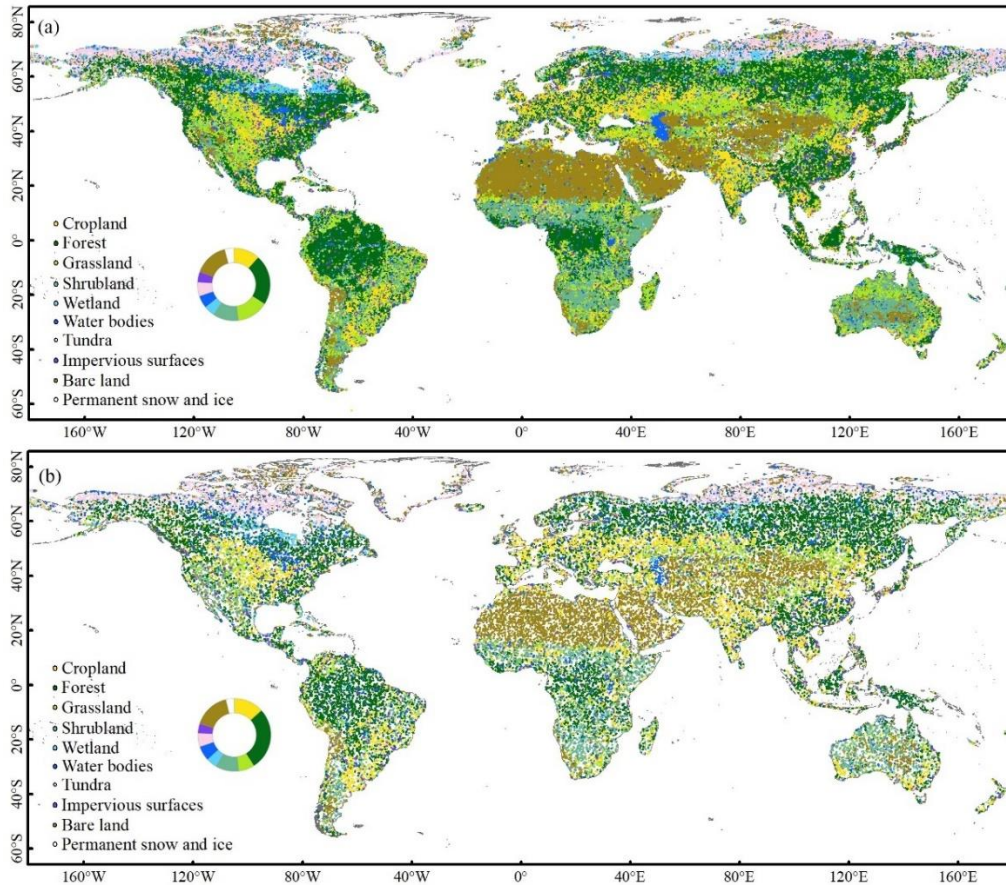
Figure 2. Spatial distribution of (a) the global point-based samples, (b) the subset of the global point-based samples for accuracy assessment and data inter-comparison, the proportions of each LC class are shown in the pie chart.

To verify the consistency between the GLC-2015 and the actual pattern of the landscape at the local scale, we also established the global patch-based samples. Simple random sampling was used to derive 5 km × 5 km blocks over the world's terrestrial area and across different ecoregions because it is easy to perform and capable to augment the sample size from target areas (Pengra et al., 2020). Since inconsistency between current GLC maps tends to appear in those heterogeneous areas, such as fragmented regions and transition zones, we slightly increased the sample size for areas with the heterogeneous landscape to better evaluate our mapping results. In total, there were 201 blocks selected as the global patch-based samples, as displayed in Figure 3a. Then, for each block in the patch-based samples, we used ArcGIS 10.5 software to derive polygons (patches) of various sizes which captured the real landscape on the high-resolution images. Meanwhile, each polygon was manually labeled with a LC class. Four examples of producing patch-based samples are shown in Figure 3b, c.

265
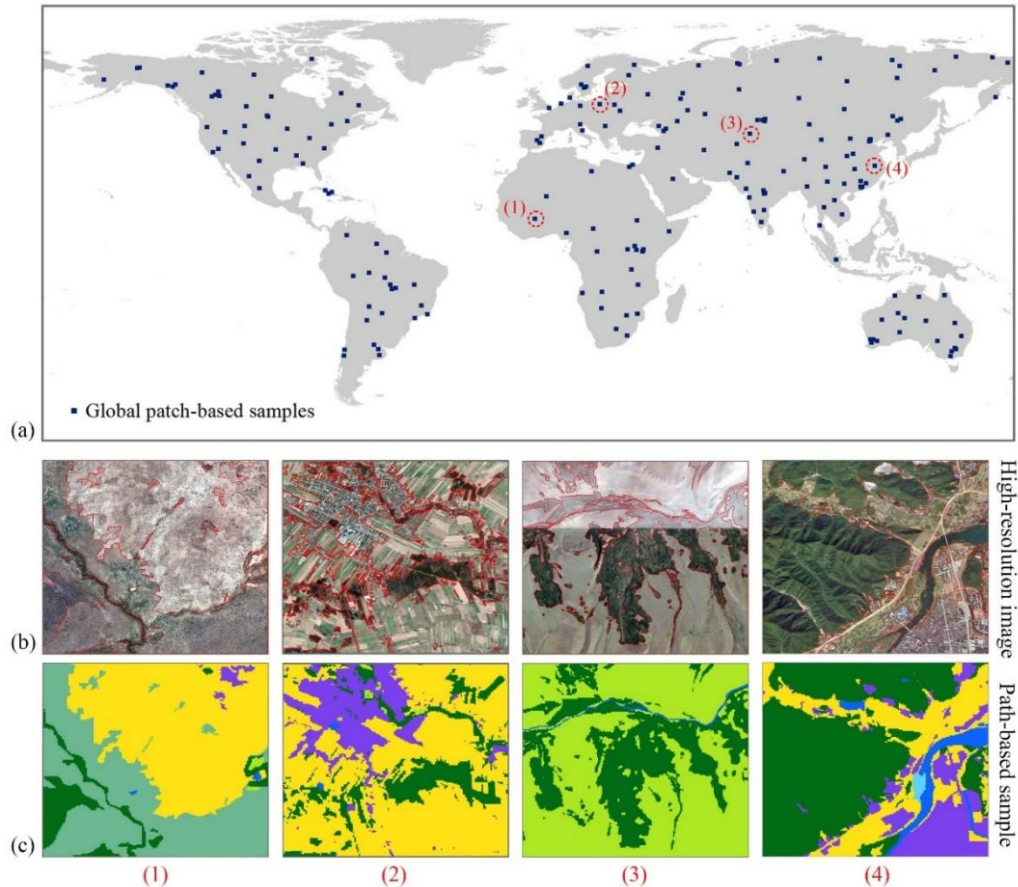
266 **Figure 3. Spatial distribution and selected examples of the global patch-based samples. The location of 5 km**

267 **× 5 km patch-based samples are shown as panel (a), the locations of four selected samples are remarked by**

268 **red dash circles. Panels (b) and (c) illustrate the production of global patch-based samples on manual**

269 **interpretation. The red lines in high-resolution images circa 2015 are results after vectorization using ArcGIS**

270 **10.5 software. Four corresponding patch-based samples are shown as (c).**

271 **3. Methods**

272 In this study, we proposed a multi-source product fusion method to produce the GLC-2015 map. The

273 procedure mainly comprised the fusion based on the Dempster-Shafer theory of evidence (DSET),

274 accuracy assessment and data inter-comparison (Figure 4). The basic of this study is the fusion of multi-

275 source GLC products based on DSET. The fusion method was performed at the pixel level and it involves

276 the following three main steps: (1) Construct the basic probability assignment (BPA) function of each

277 pixel that belongs to each LC class considering the accuracy assessment of different GLC products; (2)

278 calculate the combined probability mass for each class per pixel using the Dempster's rule of combination;

279 and (3) determine the finally accepted LC class per pixel by a decision rule. Afterwards, pixels with a

280 determined LC class were integrated to generate a new map. For large-scale or global land cover mapping,

281 previous researchers divided the study area into a lot of sub-regions and conducted classification in each

282 sub-region on GEE (Gong et al., 2020; Liu et al., 2020c; Huang et al., 2021; Jin et al., 2022; Zhang et al.,

283 2021; Zhao et al., 2021). The shape and size of sub-region vary in previous work, such as hexagons with

284 a side length of 2°, geographical grids with a size of 1°×1°, 3.5°×3.5°, 5°×5°, or 10°×10°. When deciding

285 on the size of sub-regions, two important factors should be considered. The size of samples in each sub-

286 region should be sufficient so that the rare land cover classes will not be missed. On the other hand, it is

287 impossible to implement mapping work at a sub-region as larger as we want due to memory constraints.

288 To determine the appropriate size, we tested different sizes of the sub-region (see Table S1). Result shows

289 that dividing the study area into 4°×4° grids performed best. Therefore, we split the world's terrestrial

290 area into 1507 4°×4° geographical grids. The entire framework was implemented in all 4° × 4°

291 geographical grids on the GEE platform.
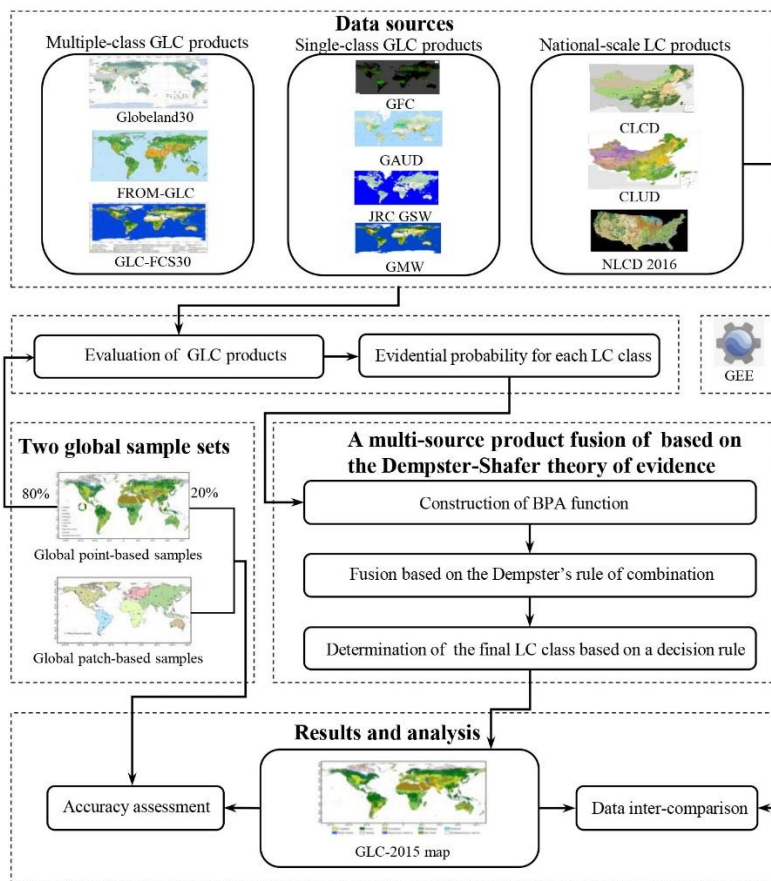
292

293 **Figure 4. The framework for generating the GLC-2015 map using a multi-source product fusion approach**

294 **based on DEST.**

295 **3.1 Definition of the classification system**

296 In this study, we adopted the classification system with 10 LC classes, including cropland, forest,

297 grassland, shrubland, wetland, water bodies, tundra, impervious surfaces, bare land, and permanent snow

298 and ice (Chen et al., 2015), as listed in Table 2. Due to the applications for different social needs, the

299 existing GLC products and national-scale LC products were produced with different classification

300 systems (Tables S2-S3). The GlobeLand30 used a simple classification system that only contained 10

301 first-level classes. Unlike the GlobeLand30, the FROM_GLC and GLC_FCS30 were classified with a

302 two-level classification scheme. Through analysis of these systems, we found that the classification

303 systems are not the same, but they have some agreements. There are both 10 major classes in the

304 GlobeLand30 and FROM_GLC despite that the definition of some classes differs. Additionally, in

305 contrast to the GlobeLand30 and FROM_GLC, the level-0 classification system of the GLC_FCS30

306 lacks tundra. However, in the level-2 detailed LC classes of the GLC_FCS30, lichens and mosses has

307 little distinction with tundra.

308 **Table 2. Classification system adopted in this paper.**

Id	LC class	Definition
10	Cropland	Land areas used for food production and animal feed.
20	Forest	Land areas dominated by trees with tree canopy cover over 30%, and sparse trees with tree canopy cover between 10%-30%.
30	Grassland	Land areas dominated by natural grass with a cover over 10%.
40	Shrubland	Land areas dominated by shrubs with a cover over 30%, including mountain shrubs, deciduous shrubs, evergreen shrubs and desert shrubs with a cover over 10%.
50	Wetland	Land areas dominated by wetland plants and water bodies.
60	Water bodies	Land areas covered with accumulated liquid water.
70	Tundra	Land areas dominated by lichen, moss, hardly perennial herb and shrubs in the polar regions.
80	Impervious surfaces	Land areas covered with artificial structures.
90	Bare land	Land areas with scarce vegetation with a cover lower than 10%.
100	Permanent snow and ice	Land areas dominated by permanent snow, glacier and icecap.

309 According to the LC translation tables (Tables S2-S3), the original LC classes of FROM_GLC and

310 GLC_FCS30, CLUD for 2015, and NLCD 2016 for 2016 were converted into the 10 target land cover

311 classes based on the similarity of LC definition. Note that cropland in our classification system was

312 defined as land areas for food production and animal feed. Therefore, pasture in level-2 classes of the

313 FROM_GLC was converted into cropland rather than grassland. In addition, lichens/mosses in the level-

314 2 detailed LC classes of GLC_FCS30 was converted into tundra.

315 **3.2 A multi-source product fusion for the GLC-2015 mapping**

316 The DSET is an effective method widely applied for the fusion of multi-source data. To generate a new

317 high-quality GLC map, a multi-source product fusion method using DSET was proposed. In the

318 remainder of the section 3.2, We introduced the overview on the theory and presented the application of

319 DSET in our mapping process.

320 **3.2.1 Dempster-Shafer theory of evidence**

321 The DSET is developed by Dempster and Shafer, which is an extension of Bayesian probability theory.

322 This theory treats information from different data sources as independent evidence and integrated these

323 evidences with no requirements regarding the prior knowledge. In the fusion, we assume a classification

324 process in which all the input data are to be classified into mutually exclusive classes. Let the set Ω of

325 these classes be a frame of discrimination. 2^{Ω} is the power set of Ω that includes all the classes and

326 their possible unions. We defined the function m: $2^{\Omega} \rightarrow [0,1]$ as the basic probability assignment (BPA)

327 function if and only if it satisfies $m(\Phi) = 0$ and $\sum_{A \subseteq 2^{\Omega}} m(A) = 1$ with $\varnothing$ denotes an empty set. For

328 each class $A \subseteq 2^{\Omega}$, m(A) is called the basic probability mass which can be computed from the BPA

329 function and represents the degree of support for class A or confidence in class A.

330   The purpose of fusion is to evaluate and integrate information from multiple sources. In the DSET,

331 these multi-source data are regarded as different evidence and provide different assessments. To generate

332 all the evidences, Dempster-Shafer theory of evidence offers a rule. Suppose $m_i(B_j)$ is the basic

333 probability mass computed from the BPA function for each input data i with $1 \leq i \leq n$ for all classes

334 $B_j \in 2^{\Omega}$. Dempster's rule of combination is provided to calculate a combined probability mass from

335 different evidences. The fusion rules are given in equation (1) and (2).

$$m(C) = \frac{\sum_{B_1 \cap B_2 \ldots \cap B_n = C} \prod_{1 \leq i \leq n} m_i(B_j)}{1 - k} \tag{1}$$

337

$$k = \sum_{B_1 \cap B_2 \ldots \cap B_n = \varnothing} \prod_{1 \leq i \leq n} m_i(B_j) \tag{2}$$

339 Where k represents the basic probability mass associated with conflicts among the sources of evidence.

340 C is the intersection of all classes B_j and carries the joint information from all the input data. After the

341 combination, we took a decision rule to decide the class we finally accept. There are several ways to

342 decide the final class by simply choosing the class with the maximum belief, plausibility, support, or

343 commonality.

344 **3.2.2 Mapping based on DSET**

345 Here, we presented our implementation for the GLC-2015 mapping in the framework of DSET. All the

346 multiple-class and single-class GLC products described in Sect. 2 were selected as input maps to be

347 combined. In the integration of multi-source GLC products, since all the LC classes in our classification

348 system are known, the frame of discrimination was defined to be our classification system:

349
$$\Omega = \left\{ \begin{array}{l} \text{cropland, forest, grassland, shrubland, wetland, water bodies,} \\ \text{tundra, impervious surfaces, bare land, permanent snow and ice} \end{array} \right\} \qquad (3)$$

350   The definition of BPA function is the critical point in applying DSET (Rottensteiner et al., 2005).

351 In the fusion, we wanted to achieve a per-pixel classification into one of ten LC classes: cropland, forest,

352 grassland, shrubland, wetland, water bodies, tundra, impervious surfaces, bare land, and permanent snow

353 and ice. For each single-class or multiple-class GLC product, the accuracy for each LC class was

354 calculated and used as evidential probability to construct the BPA. Given that the local accuracy for a

355 $4°\times4°$ grid was not able to adequately reflect the actual land cover landscape, especially for the rare LC

356 classes, the global accuracy was incorporated into the construction of the BPA to avoid uncertainties from

357 a local point of view. Since the assessment based on local samples plays a more critical role in BPA

358 construction for a local grid, a higher weight should be assigned to the local accuracy. To identify the

359 best weight, we tested different weights of the local accuracy (see Figure S1). The result shows that using

360 75% performed robustly and obtained relatively higher overall accuracy. Therefore, we chose 75% as

361 the weight for local accuracy and 25% for global accuracy. Here, we defined the BPA function as follow:

362
$$m_i(T_j) = \frac{PA_{local_{(ij)}} + UA_{local_{(ij)}}}{2} \times 75\% + \frac{PA_{global_{(ij)}} + UA_{global_{(ij)}}}{2} \times 25\% \qquad (4)$$

363 Where $m_i(T_j)$ represents the BPA function of evidence source i for the LC class T_j ; $PA_{local_{(ij)}}$,

364 $UA_{local_{(ij)}}$ denote producer's accuracy and user's accuracy of evidence source i for the LC class T_j for

365 each $4° \times 4°$ geographical grid, respectively; $PA_{global_{(ij)}}$, $UA_{global_{(ij)}}$ denote producer's accuracy and

366 user's accuracy of evidence source i for LC class T_j at the global scale.

367   To estimate the exact values of $PA_{local_{(ij)}}$, $UA_{local_{(ij)}}$, $PA_{global_{(ij)}}$ and $UA_{global_{(ij)}}$, we used 80%

368 of the global point-based samples more than 160,000 points derived in Sect 2.3. As soon as we obtained

369 the measurements of $m_i(T_j)$, the combined probability masses $m(T_j)$ were evaluated based on

370 Dempster's rule of combination for each pixel classified as the LC class T_j by fusing BPA values of all

371 the evidence sources:

$$m(T_j) = \frac{1}{1-k} \sum_{T_{1j} \cap T_{2j} \ldots \cap T_{nj} = T_j} m_i(T_j) \qquad (5)$$

372

$$k = \sum_{T_{1j} \cap T_{2j} \ldots \cap T_{nj} = \emptyset} m_i(T_j) \qquad (6)$$

373

374 Where k represents the basic probability mass associated with conflict; $m_i(T_j)$ represents the basic

375 probability mass of a certain pixel belonging to the LC class T_j from different GLC products.

376 Additionally, a belief measure (Bel) was given to measure the degree of credibility that a pixel

377 labeled as the finally accepted LC class when combining all the available evidences. The belief measure

378 was determined by

$$Bel(T_j) = \sum_{T_{ij} \subseteq T_j} m_i(T_j) \qquad (7)$$

379

380 To determine the finally accepted LC class per pixel, we took the rule of maximum combined

381 probability mass as our decision rule and the LC class with the maximum combined probability mass is

382 assigned to the 30 m pixel. Pixels labeled with the LC class were integrated to generate the GLC-2015

383 product.

384 **3.3 Accuracy assessment**

385 To assess the accuracy of the GLC-2015 map, we utilized two validation methods: validation with the

386 global point-based samples and the global patch-based samples. Since the global point-based sample set

387 is distributed evenly across the world and its sample size for each LC class is relatively sufficient and

388 balanced, even for the rare classes, it can provide a representative and credible basis for estimation of the

389 GLC-2015 map globally. Furthermore, we used the global patch-based samples to conduct accuracy

390 assessment from the local landscape scale. Although the global patch-based sample set provide an

391 inadequate sample size for rare LC classes, it can take advantage of the spatial context information and

392 efficiently reflect the actual pattern of the landscape.

393 The confusion matrix was produced to evaluate and analyze the GLC-2015 mapping result. The

394 error matrix is composed of entry A_{ij}, which represents the number of samples with reference LC class

395 j being classified as LC class i. The overall accuracy (OA), kappa coefficient, producer's accuracy (PA),

396 and user's accuracy (UA) were generated from confusion matrix to describe the quality of the GLC-2015

397 map. They are defined as follows:

$$OA = \frac{\sum_i A_{ii}}{\sum_i \sum_j A_{ij}} \tag{8}$$

398

$$P_o = OA \tag{9}$$

399

$$P_e = \sum_k \frac{\sum_i A_{ik}}{\sum_i \sum_j A_{ij}} \times \frac{\sum_j A_{kj}}{\sum_i \sum_j A_{ij}} \tag{10}$$

400

$$kappa = \frac{P_o - P_e}{1 - P_e} \tag{11}$$

401

$$PA^i = \frac{A_{ii}}{\sum_k A_{ki}} \tag{12}$$

402

$$UA^i = \frac{A_{ii}}{\sum_k A_{ik}} \tag{13}$$

403

404 Where UA^i and PA^i represent UA and PA of the LC i, respectively; P_o is the agreement between the

405 reference and the classified data; P_e is the hypothetical probability of chance agreement.

406 **3.4 Data inter-comparison**

407   To better reflect the quality of the GLC-2015 map, we intercompared the GLC-2015 map with the

408 existing LC products at multiple scales. In the accuracy assessment of different products, two global

409 validation sets described earlier were employed.

410   To figure out whether the GLC-2015 map promotes accuracy in the areas with high classification

411 difficulty and how much the improvement is compared to the existing products, we conducted the spatial

412 consistency analysis between the GlobeLand30, FROM_GLC, and GLC_FCS30 and compared the

413 mapping performance of the GLC-2015 with others in the areas of low inconsistency, moderate

414 inconsistency, and high inconsistency. To visually present the spatial consistency between three existing

415 GLC maps, we employed the spatial superposition method to obtain the spatial correspondence pixel-

416 by-pixel between different maps. Based on the times of all the GLC products agreed for the same LC

417 class, the degree of consistency for a pixel was identified as three levels with the agreement value equal

418 to 3, 2, or 1. The areas of low inconsistency were regarded as pixels that classified as the same LC class

419 in all three GLC maps (labeled as 3). The moderate inconsistency areas were regarded as pixels that were

420 consistent in only two GLC maps (labeled as 2). The high inconsistency areas were regarded as pixels

421 that were totally inconsistent in these three GLC maps (labeled as 1). For a visual comparison, all these

422   GLC maps were aggregated to 0.05°, in which the LC class with the largest proportion determined the

423   class in each 0.05° grid.

424   **3.5 Assessment on mapping performance of DSET and other methods**

425   In addition to inter-comparison between the GLC-2015 map and three existing GLC products, we

426   compared the DSET method with two existing commonly used fusion methods, including the majority

427   voting (MV) and spatial correspondence (SC) based on two global validation sets including 20% of the

428   global point-based samples and the whole global patch-based samples. MV is a fusion approach that

429   combines input maps and adopts the LC class favored by the majority of the candidate maps. In the MV

430   method, we compared the GlobeLand30, FROM_GLC, and GLC_FCS30 at each pixel and chose the

431   class that two or three LC products agreed for. For pixels where three LC products were different, the

432   LC class of the product with the highest accuracy was adopted. SC method produces an integrated land

433   cover map by selecting the LC class of the input map that has the highest spatial correspondence with

434   the reference data. In this study, 80% of the global point-based samples were used as the reference data

435   to obtain the SC map of each global LC product. If the class of a product agreed with that of the point-

436   based sample, a value equal to 1 was assigned to that sample. On the contrary, a value equal to 0 was

437   assigned to the sample if the class of the product differed from that of the sample. In each 4° × 4° grid,

438   we used the Kriging method to obtain spatial correspondence maps which have the correspondence value

439   ranging from 0 to 1 for three products. Then, the class of the product with the highest spatial

440   correspondence was chosen for each pixel.

441   Furthermore, we compared the mapping performance of DSET with Random Forest (RF) which is

442   considered one of the most popular algorithms for land cover mapping. In the land cover classification

443   using the FR classifier, all available Level-2 Tier 1surface reflectance (SR) data of Landsat 8 OLI

444   (Operational Land Imager) sensors from the year 2015 and two adjacent years on GEE was employed.

445   All Landsat images have been atmospherically corrected. The following six bands were used as input

446   features: blue, green, red, NIR, SWIR1, and SWIR2. To improve the mapping performance, several

447   important spectral indices, including DNVI, NDWI, and NDBI were also used as auxiliary data to the

448   RF classifier. The RF classifier was trained on 80% of the global point-based samples since those samples

449   were of high quality after manual visual interpretation of high-resolution images. As the global land cover

450   mapping based on the RF classifier is a tough task, we randomly selected a total of 300 grids with the

451 size of 4° (Figure S2) and applied corresponding local RF classifiers to these grids. Then, the mapping

452 results were validated by the remaining 20% of the point-based samples.

4. Results and discussion

4.1 Mapping result of the GLC-2015 map

Using a multi-source product fusion method based on the DSET, we generated an improved 30m global

land cover map in 2015 (GLC-2015). Figure 5 illustrates the GLC-2015 map. The GLC-2015 map can

accurately describe the spatial distribution of various LC classes. For example, cropland areas are mostly

located in Central America, the region from the Hungarian plain to the Siberian plain, the eastern and

southern parts of China, and the most of India. In addition, forest, which is one of the easily

distinguishable classes from the map, is concentrated in the eastern part of North America, the Amazon

basin of South America, the northern part of Eurasia and the equatorial region of Africa.
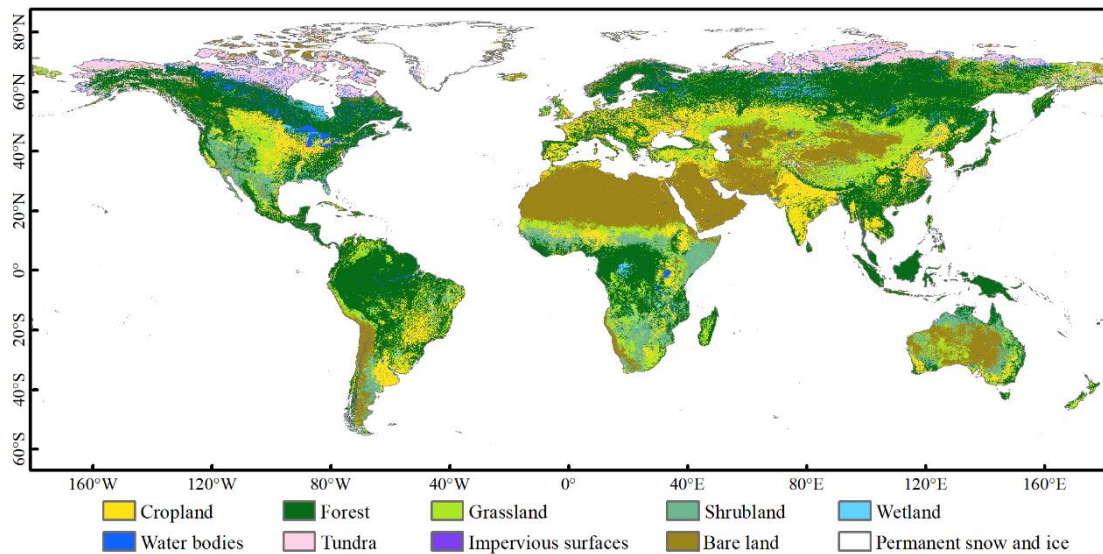
Figure 5. Global land cover map in 2015 with 30 m resolution (GLC-2015).

4.2 Accuracy assessment of the GLC-2015 map

4.2.1 Accuracy assessment with the global point-based samples

The accuracy of the GLC-2015 map was first tested via the global point-based samples, and the results

of assessment are listed in Table 3. The GLC-2015 map achieved an OA of 79.5% and kappa coefficient

of 0.757 at the global scale, demonstrating the good performance of our map. Among all the LC classes,

permanent snow and ice possessed the best mapping performance, with PA and UA achieving 89.1% and

470 93.7%. The accuracy of water bodies, forest and impervious surfaces was also high, where PA and UA

471 exceeded 80.0%. Grassland, shrubland, and wetland had relatively low accuracy, with PA below 75.0%.

472 Among them, grassland and shrubland were mainly confused with forest, which might be because these

473 classes are both vegetation, thus causing difficulty in recognition by spectral information. Due to the

474 complex spectral characteristics, wetland is often mixed with vegetation (Ludwig et al., 2019).

475 **Table 3. The confusion matrix for the GLC-2015 map based on the global point-based samples.**

	Cropland	Forest	Grassland	Shrubland	Wetland	Water bodies	Tundra	Impervious surfaces	Bare land	Permanent snow and ice	Total	PA
Cropland	3623	387	356	61	27	48	2	71	81	0	4656	0.778
Forest	155	8813	186	141	232	16	43	43	53	3	9685	0.910
Grassland	10	337	1920	19	24	13	47	36	184	9	2599	0.739
Shrubland	155	438	656	1469	39	29	70	78	442	4	3380	0.435
Wetland	47	287	82	14	1067	64	22	18	110	4	1715	0.622
Water bodies	27	90	15	1	73	1936	17	10	44	3	2216	0.874
Tundra	1	242	119	6	29	19	1411	2	269	17	2115	0.667
Impervious surfaces	74	41	11	3	8	11	1	1295	45	0	1489	0.870
Bare land	36	59	237	32	44	91	55	60	4909	38	5561	0.883
Permanent snow and ice	0	11	8	0	4	18	13	1	86	1154	1295	0.891
Total	4128	10705	3590	1746	1547	2245	1681	1614	6223	1232	34711	
UA	0.878	0.823	0.535	0.841	0.690	0.862	0.839	0.802	0.789	0.937		
OA						0.795						
Kappa						0.757						

476 The regional accuracies are presented in Figure 6. The OA of the GLC-2015 ranged from 66.4% to

477 93.4%, and kappa coefficient from 0.552 to 0.813. From the perspective of OA, Water regions lead,

478 followed by Tropical desert, Temperate continental forest, and Polar. These are areas with homogeneous

479 land cover and have low difficulty in mapping. Boreal tundra woodland, Tropical dry forest, Tropical

480 shrubland, and Subtropical desert are the regions with low OA. The first one may be related to the high

481 latitudes. The followed two may be because they belong to areas with complicated and mixed LC classes

482 which is not easily classified. The last one may be the consequence of sparse vegetation in desert areas.

483   For the kappa coefficient, the ranking was similar with those for OA.

484
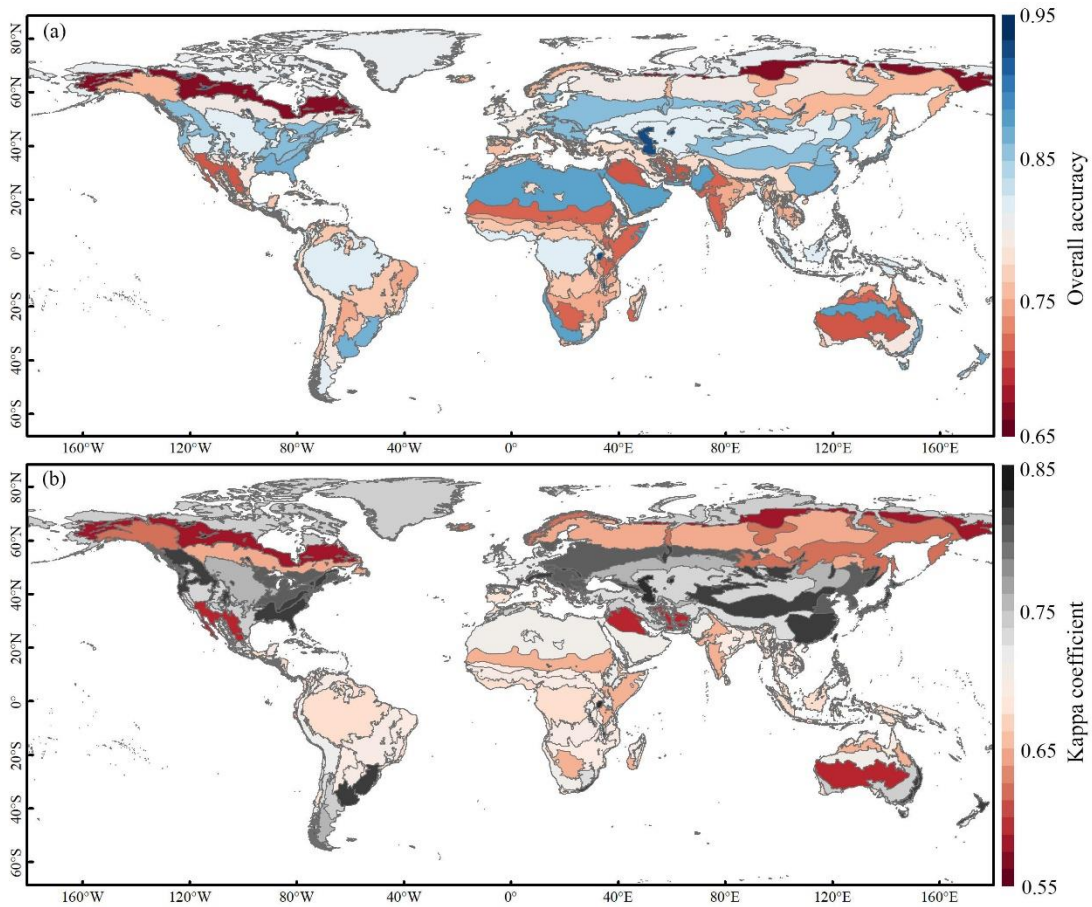
Figure 6. Regional accuracy of the GLC-2015 map according to ecoregions. (a)overall accuracy, (b) kappa coefficient. The ecoregion boundaries are obtained from the Food and Agriculture Organization of the United Nations (FAO).

4.2.2 Accuracy assessment with the global patch-based samples

The accuracy assessment of the GLC-2015 map was also conducted with the global patch-based samples. Table 4 summarizes the results for accuracy assessment of each LC class in the GLC-2015 map. From the assessment results, it can be found that the OA of the GLC-2015 map reached 83.6%, which was higher than 79.5% tested with the global point-based samples. The kappa coefficient of the GLC-2015 map was 0.566, which was 0.191 lower than the result calculated with the global point-based samples. In both accuracy assessment results based on two different validation data sets, water bodies, forest, and permanent snow and ice were validated to have high accuracy, and grassland, shrubland, and wetland were validated to have low accuracy. Nevertheless, the ranking of accuracy for each LC class had a slight difference. For example, in assessment based on the global point-based samples, impervious surfaces and permanent snow and ice ranked higher than that based on the global patch-based samples. This may

499 be because a LC map can easily show where one LC class is distributed but hardly describe its actual

500 shape. In addition to the accuracy assessment on a pixel scale, validation on a patch scale is equally

501 important because it can reflect the shape consistency between the GLC-2015 map and the actual

502 landscape, even if the size of global patch-based samples is relatively small. Overall, no matter from the

503 respective of the global point-based samples or the global patch-based samples, the mapping accuracies

504 of the GLC-2015 map are satisfactory.

505 **Table 4. Mapping accuracy via the global patch-based samples for the GLC-2015 map**

	Cropland	Forest	Grassland	shrubland	Wetland	Water bodies	Tundra	Impervious surfaces	Bare land	Permanent snow and ice
PA	0.887	0.895	0.629	0.589	0.301	0.939	0.701	0.757	0.682	0.825
UA	0.916	0.844	0.617	0.714	0.511	0.917	0.872	0.713	0.599	0.767
OA						0.836				
Kappa						0.566				

506 **4.3 Inter-comparison with existing GLC products**

507 **4.3.1 Inter-comparison based on the global point-based samples**

508 Based on the global point-based samples, the inter-comparison of the GLC-2015 map with the

509 GlobeLand30, FROM_GLC, and GLC_FCS30 were conducted. Since the three products used different

510 classification systems, LC classes were transformed to the classification system we adopted in this paper

511 to achieve consistent accuracy assessment. The accuracy assessment results for all GLC maps are listed

512 in Table 5. It can be found that the GLC-2015 map achieved the highest OA of 79.5% compared with

513 GlobeLand30 of 65.3%, FROM_GLC of 61.7%, and GLC_FCS30 of 65.5%, respectively. The accuracy

514 gap between the GLC-2015 map and other existing ones was 14.0%-17.8%. Also, the GLC-2015 map

515 possessed a better kappa coefficient than other products. For each LC class, the GLC-2015 map

516 outperformed the other three maps in terms of PA except for tundra. For cropland, grassland, shrubland,

517 wetland, and tundra, the GLC-2015 map also exhibited better performance for UA than the GlobeLand30,

518 FROM_GLC and GLC_FCS30. Overall, for the PA or UA, the GLC-2015 map ranked first or second in

519 nearly all LC classes, which demonstrated that the GLC-2015 map had smaller omission and commission

520 errors against the other three products.

521 **Table 5. Mapping accuracy of the GLC products with the global point-based samples.**

		Cropland	Forest	Grassland	Shrubland	Wetland	Water bodies	Tundra	Impervious surfaces	Bare land	Permanent snow and ice	OA (Kappa coefficient)
GLC-2015	PA	0.778	0.910	0.739	0.435	0.622	0.874	0.667	0.870	0.883	0.891	0.795
	UA	0.878	0.823	0.535	0.841	0.690	0.862	0.839	0.802	0.789	0.937	(0.757)
Globeland30	PA	0.752	0.719	0.713	0.245	0.540	0.680	0.769	0.688	0.609	0.821	0.653
	UA	0.786	0.818	0.255	0.428	0.573	0.869	0.577	0.809	0.868	0.905	(0.598)
FROM_GLC	PA	0.389	0.694	0.707	0.411	0.307	0.607	0.712	0.732	0.731	0.881	0.617
	UA	0.671	0.859	0.278	0.422	0.289	0.742	0.686	0.661	0.761	0.773	(0.558)
GLC_FCS30	PA	0.757	0.775	0.452	0.399	0.455	0.604	0.228	0.777	0.809	0.726	0.655
	UA	0.616	0.816	0.384	0.405	0.515	0.808	0.688	0.774	0.645	0.947	(0.591)

522   Further quantitative accuracy assessments of different GLC products were performed in 4° × 4°

523   grids using the global point-based samples, and box plots were produced for each product for all grids

524   within different ecoregions, as shown in Figure 7. It can be found that the GLC-2015 map outperformed

525   other existing products with the best OA and kappa coefficient across different ecoregions. Also, the

526   mean overall accuracy of the GLC-2015 map exceeded 65.0% in all ecoregions, showing the high quality

527   of our mapping results. It is worth noting that the GLC-2015 map showed shorter boxes except in

528   Subtropical dry forest and Subtropical desert, which means the GLC-2015 map had relatively small

529   fluctuation than other ones. In Subtropical desert, Tropical dry forest, and Boreal tundra woodland, the

530   OA and kappa coefficient of the four products were relatively low. However, the GLC-2015 map

531   exceeded the highest of others and greatly improved the mean OA in these regions.
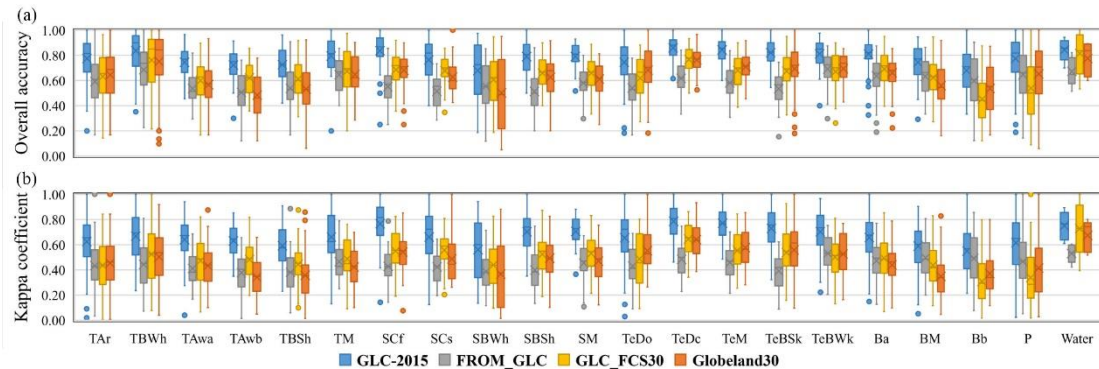
532

533 **Figure 7. The box-plot of the accuracy for twenty-one ecoregion zones. (a) overall accuracy, (b)kappa**

534 **coefficient. Ecoregion abbreviation and corresponding ecoregion is described in Table S4.**

 4.3.2 Inter-comparison based on the global patch-based samples

536 Although the global point-based samples are adequate and even across the globe, the distribution of

537 points in each 4° × 4° geographical grid is too sparse to reflect the actual spatial pattern of the landscape.

538 Focusing on LC pattern at the local scale, we also used the global patch-based samples which can provide

539 spatial context information to conduct the accuracy assessment of the GLC-2015 map and compare

540 difference GLC products. Table 6 lists the accuracies of the GLC-2015 map and the other three GLC

541 products. Obviously, the GLC-2015 map achieved the best OA and kappa coefficient among these four

542 GLC maps. The overall accuracy gap between the GLC-2015 product and others was 5.9%-24.5%, which

543 presented a more significant variation compared with the result based on the global point-based samples.

544 In terms of PA and UA, the GLC-2015 map was higher than the other three ones in most LC classes.

545 Specifically, all the products had lower accuracy for grassland, shrubland, and wetland, similar to that in

546 the accuracy assessment based on the global point-based samples. It is evident that the FROM_GLC had

547 the lowest mapping accuracy for grassland, shrubland, and wetland, implying that the classification

548 method of FROM_GLC is not robust for these three LC classes.

549 **Table 6. Mapping accuracy of the GLC products with the global patch-based samples**

		Cropland	Forest	Grassland	Shrubland	Wetland	Water bodies	Tundra	Impervious surfaces	Bare land	Permanent snow and ice	OA
GLC-2015	PA	0.887	0.895	0.629	0.589	0.301	0.939	0.701	0.757	0.682	0.825	0.836
	UA	0.916	0.844	0.617	0.714	0.511	0.917	0.872	0.713	0.599	0.767	(0.566)
Globeland30	PA	0.896	0.698	0.765	0.539	0.455	0.824	0.752	0.643	0.492	0.831	0.777
	UA	0.891	0.906	0.444	0.527	0.157	0.893	0.500	0.703	0.829	0.705	(0.437)
FROM_GLC	PA	0.485	0.714	0.640	0.254	0.032	0.904	0.760	0.506	0.681	0.501	0.591
	UA	0.872	0.809	0.193	0.139	0.186	0.884	0.696	0.808	0.496	0.703	(0.360)
GLC_FCS30	PA	0.865	0.779	0.398	0.565	0.363	0.869	0.051	0.648	0.658	0.742	0.748
	UA	0.857	0.832	0.509	0.330	0.132	0.942	0.573	0.643	0.462	0.752	(0.418)

550 Accuracy assessment was calculated in each patch-based sample, and box plots were produced for

551 each GLC product at the continental scale, as shown in Figure 8. The GLC-2015 map showed a robust

552 performance in each continent, with the highest OA and kappa coefficient among all the maps. Also, in

553 all continents, the GLC-2015 map had the shortest boxes in terms of OA, which denoted that it had a

554 more minor variation in accuracy at the continental scale. Among four products, the GLC_FCS30 and

555 Globeland30 achieved similar accuracies in most continents. Obviously, the FROM_GLC showed lowest

556 accuracy across different continents, especially in Oceania, where the OA of most patch-based samples

557 was below 40.0%, namely most of the pixels in Oceania were incorrectly classified. We further compared

558 mapping accuracies for each LC class in different continents (Figures S3-S4). Since tundra and

559 permanent snow and ice are rare and only existent in certain regions, they were not included in the

560 comparison. As for PA across different continents, the GLC-2015 map outperformed other maps in forest,

561 water bodies, and bare land. As for UA across different continents, the GLC-2015 map outperformed

562 other maps in cropland, grassland, shrubland and wetland, and achieved similar accuracies with the

563 GLC_FCS30 and Globeland30 in forest. Overall, the GLC-2015 map outperformed others regarding

564 mapping accuracy at continental scale. In addition, all GLC products showed significant variation and

565 low mean accuracy in grassland, shrubland, and wetland over most continents.
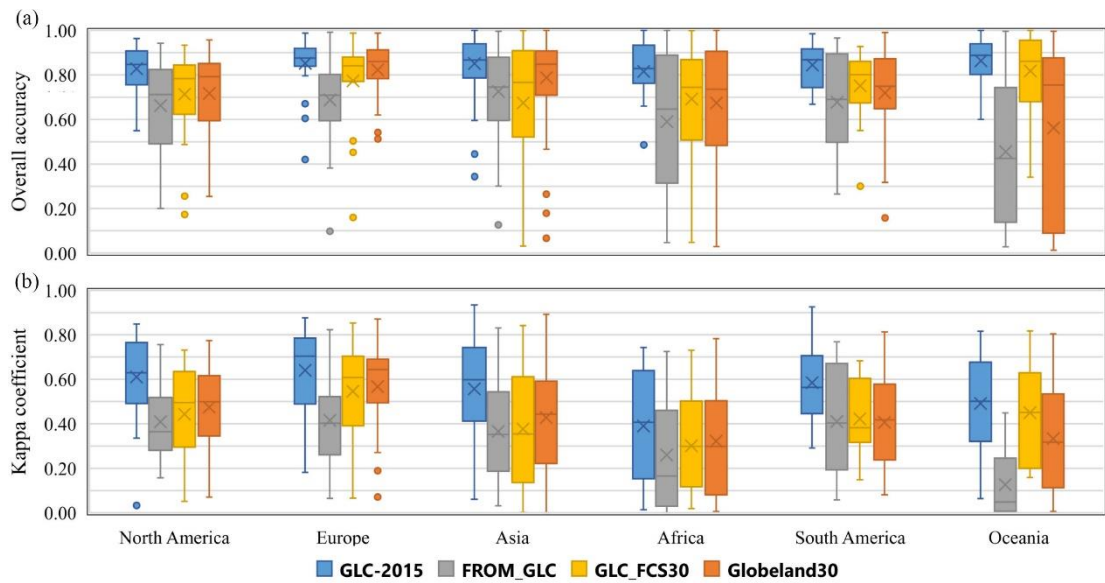
566

567 **Figure 8. The box-plot of the accuracy for different continents. (a) overall accuracy, (b)kappa coefficient.**

568   Furthermore, to compare the OA of the GLC-2015 map with other GLC products, scatter plots were

569 used to describe the relationship between the overall accuracy of the GLC-2015 map and one other

570 product in each patch-based sample, as displayed in Figure 9. Most of the points were above the 1:1 line,

571 implying that the GLC-2015 map surpassed other GLC products in terms of OA. The distribution of

572 points was more dispersed from the 1:1 line in the plot of the GLC-2015 map against FROM_GLC

573 compared to other plots. It indicated that these two products had a more significant difference, which

574 was also proved in Table 6.

575
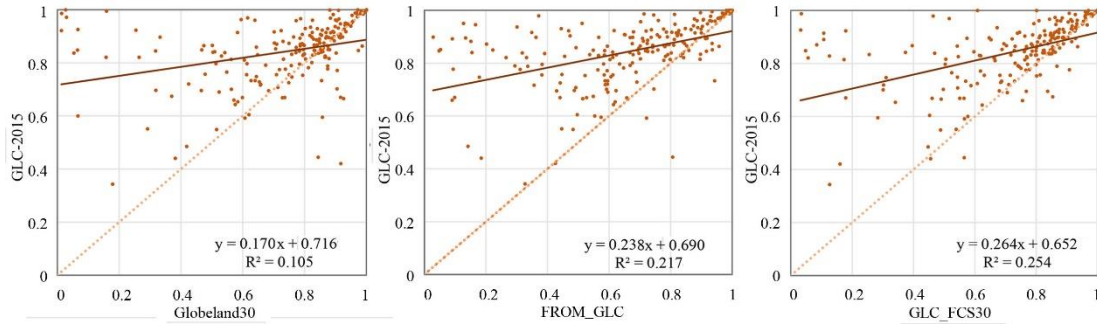
Figure 9. Scatter plots between the GLC-2015 map and other products obtained using the global patch-based

samples.

4.3.3 Areal comparison for individual classes

To assess the similarities and discrepancies between the GLC-2015 and other GLC products, we

compared the area of various LC classes at multiple scales, including global, continental, national, and

ecoregional scales.

The areal comparison for various classes of different GLC products over the globe is shown in

Figure 10. Generally, the areas of water bodies and permanent snow and ice of four GLC products were

very similar, which may be related to the similar LC definitions. In contrast, the areas of cropland, forest,

grassland, and shrubland in GLC-2015 differed significantly from those in other GLC products. The area

of forest in GLC-2015 is much higher than other products. This may be because FROM_GLC and

GLC_FCS30 defined forest with tree cover over 15%, while GLC-2015 used a threshold of over 10%.

The cropland areas in GLC-2015 and Globeland30 were close, higher than FROM_GLC but lower than

GLC_FCS30. Moreover, the FROM_GLC underestimated the cropland area as it had a low producer's

accuracy for cropland (see Table 5), which was also demonstrated in previous researches (Liu and Xu,

2021; Zhang et al., 2021). FROM_GLC and Globeland30 shared similar grassland areas since a similar

accuracy for grassland was found in these two products (see Table 5). However, the FROM_GLC and

Globeland30 significantly overestimated grassland extent, with much bare land misclassified as

grassland (Hu et al., 2014). The GLC_FCS30 showed the smallest area for grassland, which might be

related to its higher threshold in vegetation cover for grassland. For shrubland, the area difference

between GLC-2015 and Globeland30 was minimal, and the areas in FROM_GLC and GLC_FCS30 were

similar. Furthermore, the wetland area in FROM_GLC was the lowest among all the products, with a

total area of 0.168 million km^2. In contrast, the Globeland30 and GLC_FCS30 exhibited greater wetland

extent than GLC-2015 since these two products classified non-wetlands sensitive to water as wetlands

600 (Zhang et al., 2023). In particular, the tundra area in GLC_FCS30 was much smaller than other products.

601 This is mainly because only lichens/mosses in the original classification system of GLC_FCS30 was

602 converted into tundra in the classification system we used, which leads to the omission of tundra. The

603 areas of impervious surfaces in GLC-2015, Globeland30, and GLC_FCS30 were very close and higher

604 than FROM_GLC. For bare land, there was large difference between Globeland30 and other products,

605 while the area in GLC-2015 and GLC_FCS30 was very close.

606
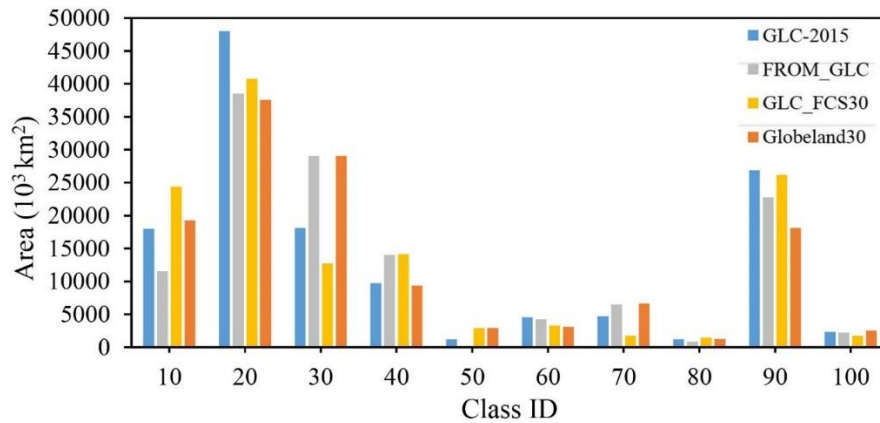
Figure 10. Areal comparison of various land cover classes among GLC products at the global scale. Class IDs
10, 20, 30, 40, 50, 60, 70, 80, 90, and 100 denote cropland, forest, grassland, shrubland, wetland, water bodies,
tundra, impervious surfaces, bare land, and permanent snow and sea ice, respectively.

610   The area similarity and difference for various classes of different GLC products were also compared

611 over six continents, the top 40 countries ranked by area, and 21 ecoregions (Figures S5-S7). Overall, the

612 four products showed a similar distribution trend of different classes. For most LC classes, the continental,

613 national, and ecoregional rankings of four products agreed with their ranking at the global scale. Whereas,

614 for grassland and shrubland, the area ranking of four products varied at three different regional scales.

615 **4.3.4 Visual inter-comparison for individual classes**

616 The visual comparison of cropland in GLC-2015, Globeland30, FROM_GLC, GLC_FCS30, Global

617 Food Security-Support Analysis Data (GSFAD30) (Xiong et al., 2017; Teluguntla et al., 2018), and other

618 national-scale maps was conducted in three local regions (Figure S8). In the Egyptian agricultural area,

619 GLC-2015, FROM_GLC, and GLC-FCS30 shared similar delineation of the cropland and had a good

620 representation of cropland with fine spatial details. Since the date time of the Google Earth image is 2015,

621 Globeland30 missed the newly cultivated cropland. GFASD30 had the largest cropland area among five

622 products but misclassified bare land as cropland. In the agricultural area of Southeastern China, GLC-

623 2015 had an agreement with GFSAD30 and CLCD. Globeland30 and GLC_FCS30 overestimated the

624 area of cropland. As for FROM_GLC, it failed to depict the spatial distribution of cropland and had many

625 omissions. In cropland-dominated areas of the United States, FROM_GLC significantly underestimated

626 the extent of cropland. The other five products exhibited a similar delineation of cropland, but there were

627 little differences in some small areas. For example, Globeland30 misclassified some grassland into

628 cropland, and NLCD 2016 had a good ability to distinguish the farm rack.

629   We also compared the performance in the forest of different products in three forest-prevalent

630 regions of Congo, China, and the United States (Figure S9). Overall, GLC-2015 and Globeland30

631 showed accurate delineation in three regions. FROM_GLC also had good performance for the forest in

632 Congo and USA but overestimated the forest in China, mislabeling shrubland and grassland as forest.

633 Furthermore, GFC tended to miss sparse trees in China, and GLC_FCS30 underestimated the extent of

634 forest in both three regions. As for national-scale products, CLCD and NLCD 2016 had a good ability to

635 identify the details of forest, while CLUD dramatically missed both dense and sparse woodlands.

636   Furthermore, to compare the performance in the wetland of GLC-2015 with other global and

637 national-scale products, three wetland regions in South-central Canada, coastal America, and Sundarbans

638 were selected. It can be found that GLC-2015 and Globeland30 had similar representation and performed

639 well in identifying the wetland over three regions (Figure S10). Unexpectedly, FROM_GLC performed

640 poorly in each region, with almost no wetlands captured. GLC_FCS30 also showed unstable quality in

641 three regions. For example, it highly underestimated the wetland area in coastal America and completely

642 mislabeled the mangroves as cropland in Sundarbans. NLCD 2016 and GMW accurately demonstrated

643 the spatial pattern of the wetland, while the CA_wetlands map underestimated the wetland extent because

644 it defined wetlands by wetland frequency of no less than 80% from 2000 to 2016 (Wulder et al., 2018).

645   To understand the spatial distribution of impervious surfaces in different products, a comparison of

646 mapping results for three megacities, including Tokyo, Shanghai, and New York, was shown in Figure

647 S11. In Tokyo, a high consistency was found between GLC-2015, FROM_GLC, and GAUD, and both

648 successfully captured the impervious surfaces in peri-urban areas. GLC_FCS30 showed the largest area

649 for impervious surfaces because it misclassified many croplands into impervious surfaces. In Shanghai,

650 GLC_FCS30 underestimated the central city, and CLUD lost the details of impervious surfaces because

651 it was developed using the visual interpretation method. Other products generally had the similar

representation and accurately demonstrated the spatial distribution of the city. For New York, the FROM_GLC, GLC_FCS30, and GAUD agreed well with GLC-2015, while Globeland30 and NLCD 2016 had high impervious areas than others.

4.3.5 Visual inter-comparison at the local scale

We selected six typical geographical tiles covering six continents and different landscape environments to further present the mapping performance of the GLC-2015 map, Globeland30, FROM_GLC, and GLC_FCS30, as shown in Figure 11. Overall, from a local point of view, the GLC-2015 map tended to be more diverse in LC classes and had better identification performance in various classes. In flattened cropland areas (Figure 11a and Figure 11b), the GLC-2015 map revealed diverse LC classes and accurately distinguished impervious surfaces; however, the Globeland30 exaggerated the extent of impervious surfaces, and the FROM_GLC failed to delineate impervious surfaces with small size. In addition, the FROM_GLC misclassified some cropland pixels as grassland (Figure 11a) and had an abnormal "stamp" (Figure 11b). As for mountain areas (Figure 11c and Figure 11d), the GLC-2015 map uncovered the spatial pattern of natural and planted forest, cropland, and grassland. There were large confusions between cropland and grassland in the results of the FROM_GLC and GLC_FCS30, and some impervious surfaces and cropland areas were wrongly labeled as bare land by the FROM_GLC. The areas (Figure 11c), which were classified as forest, were misidentified as cropland and grassland in three other products. For the rainforest areas where a large number of trees were reclaimed for cropland (Figure 11e), the GLC-2015 map, Globeland30, and GLC_FCS30 had similarities in cropland areas; but the FROM_GLC recognized some reclaimed areas as grassland. Additionally, the GLC-2015 map accurately presented the spatial distribution of impervious surfaces while other products had omission or commission errors. In the cropland-dominated areas (Figure 11f), the GLC-2015 map and Globeland30 showed a higher agreement, and both of them mapped the undulating areas as grassland. Unlike the aforementioned two products, the FROM_GLC misclassified large tracts of croplands as grasslands, and the GLC_FCS30 did not capture the grassland in undulating areas. Figure 11 also shows the belief measure of the fused result in different geographical tiles. Although it does not directly evaluate the mapping accuracy, it serves as a degree of support for the hypothesis of an accepted LC class being true, it can still reflect the quality of the GLC-2015 map. Overall, Bel of the GLC-2015 map exceeded 80% in most areas of each tile, demonstrating the credibility and high quality of our mapping result.

| Google Earth image | GLC-2015 | Globeland30 | FROM_GLC | GLC_FCS30 | Bel |

Legend:
Cropland, Forest, Grassland, Shrubland, Wetland, Water bodies, Tundra, Impervious surfaces, Bare land, Permanent snow and ice, 30 50 70 100(%)

681
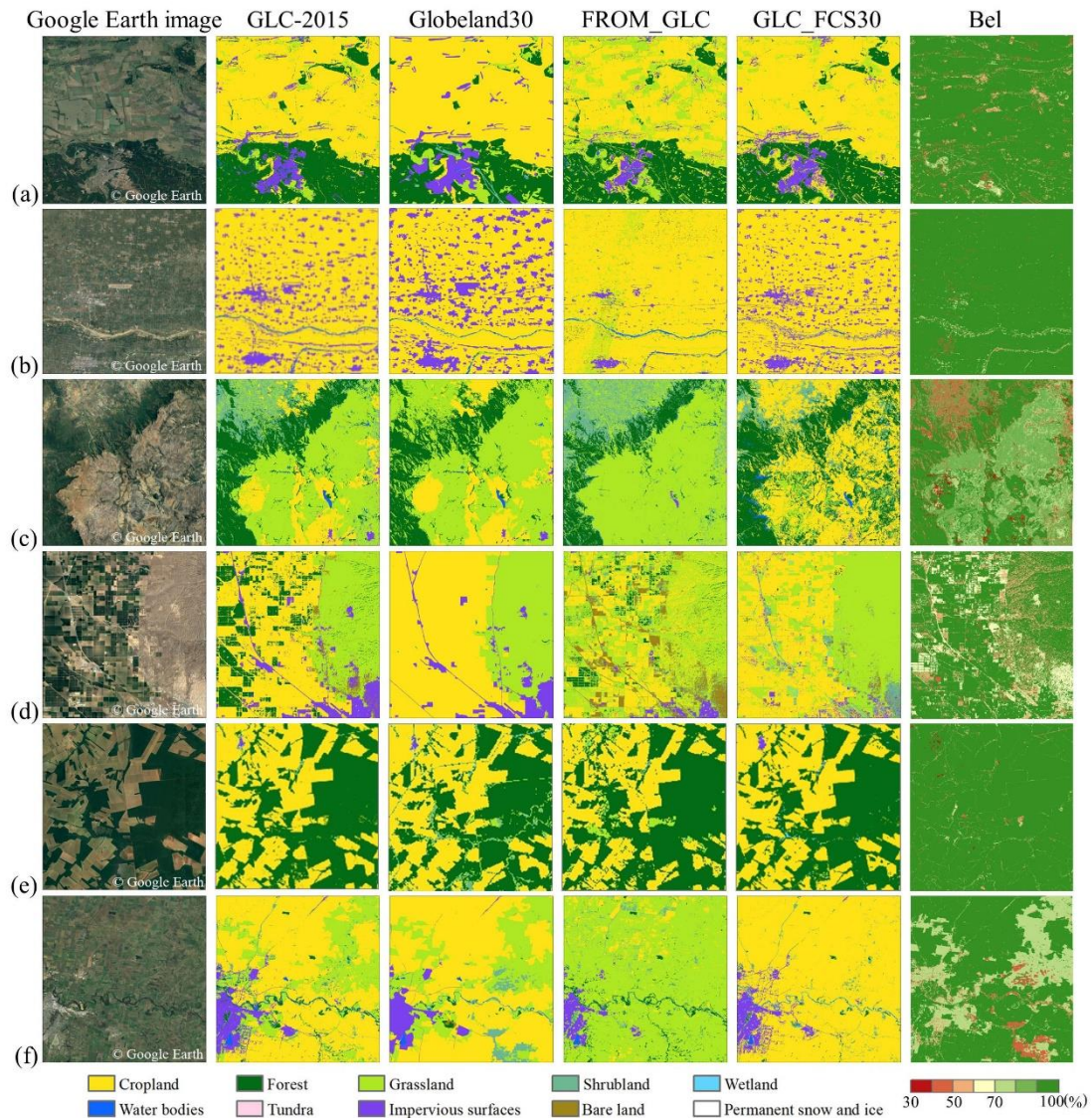
Figure 11. Visual comparison between the GLC-2015 map and three other products for different continents.
(a) to (f) are examples for Europe, Asia, Africa, North America, South America, and Oceania, respectively.

4.4 Inter-comparison with national-scale products

Except for comparison with the existing GLC products, the GLC-2015 was also compared with three national-scale products (CLCD, CLUD, and NLCD 2016 over CONUS). We first compared the accuracy of the GLC-2015 with NLCD, CLCD, and CLUD using the point-based samples (Tables S5-S6). It can be found that the GLC-2015 obtained an overall accuracy of 88.8% in China, higher than CLCD (78.3%) and CLUD (70.2%). Specifically, the GLC-2015 achieved the highest PA and UA in all LC classes except wetland. In the CONUS, the GLC-2015 outperformed NCLD 2016 with an OA improvement of 13.2%. Additionally, the GLC-2015 exhibited better mapping performance in nearly all LC classes.

693   An accuracy comparison between the GLC-2015 and three national-scale products was also

694   performed using the patch-based samples (Tables S7-S8). Overall, the GLC-2015 achieved a better OA

695   of 85.7% in China, with respect to CLCD (83.6%) and CLUD (75.4%). In terms of PA and UA, the GLC-

696   2015 ranked first or second in most LC classes. In the CONUS, the GLC-2015 possessed an OA of 84.5%

697   and a kappa coefficient of 0.787, outperforming NLCD 2016. Although the GLC-2015 had lower PAs in

698   wetland and impervious surfaces, and lower UAs in cropland and forest compared to NLCD 2016, the

699   GLC-2015 outperformed NLCD 2016 in most LC classes.

700   We further performed an areal comparison for each LC class of GLC-2015 and three national-scale

701   products (Figures S12-S13). Generally, the GLC-2015, CLCD, and CLUD exhibited similar areas in

702   most classes. Notably, the areas of cropland, shrubland, and wetland in GLC-2015 were very close to

703   CLCD but different from CLUD. In the CONUS, the areas of cropland, water bodies, and bare land in

704   the GLC-2015 and NLCD 2016 were close. In contrast, the areas of the remaining LC classes in the

705   GLC-2015 showed a large difference from NLCD 2016. The area differences in forest, grassland and

706   shrubland between GLC-2015 and NLCD 2016 were mainly related to different LC definitions. For

707   example, the minimum fraction of tree cover in the forest is 10% in GLC-2015, whereas NLCD 2016

708   used a minimum fraction of 20%. NCLD 2016 had higher area of impervious surfaces than the GLC-

709   2015 because open urban in NLCD 2016 includes too much vegetation.

710   **4.5 Improvement of the GLC-2015 map compared to existing GLC products**

711   The spatial distribution of inconsistency between three GLC products at the global scale is illustrated in

712   Figure 12. From the inconsistency map, we found that areas of low inconsistency mainly corresponded

713   to homogeneous regions with simple LC classes. For example, the northern part of Africa was mainly

714   classified as bare land, the northern part of South America was mainly classified as forest, and the

715   Greenland was classified as permanent snow and ice. On the contrary, areas of high inconsistency were

716   located in regions with complicated LC classes, especially in mixed vegetation regions or sparse

717   vegetation regions, such as northern Asia, South Africa, Sahel region, Australia, northern and southern

718   North America, and eastern and southern South America.
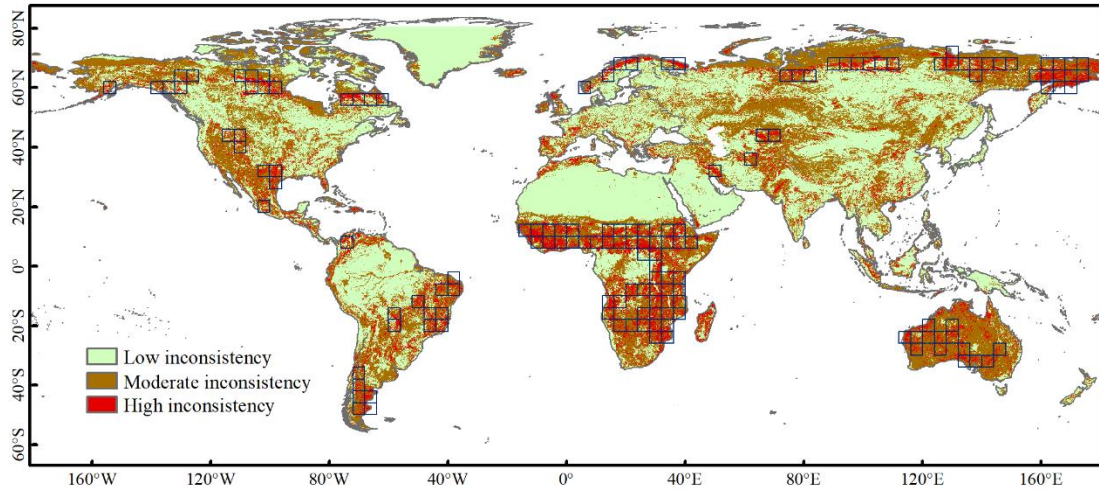
719

720 **Figure 12. Distribution of inconsistency between the Globeland30, FROM_GLC, and GLC_FCS30.The blue**
721 **rectangles are high-inconsistency grids that the area of pixels with value equal to 1 account for more than 20%**
722 **of the total area.**

723   Based on the global point-based samples, we assessed the accuracies of the GLC-2015 map,

724 Globeland30, FROM_GLC, and GLC_FCS30, in the aforementioned areas of low inconsistency,

725 moderate inconsistency, and high inconsistency, as shown in Table 7. Overall, the GLC-2015 map had

726 the highest accuracies against the other three ones in three areas. For each product, areas of low

727 inconsistency obtained the highest accuracies, followed by areas of moderate inconsistency and then high

728 inconsistency, which demonstrated that inconsistency of the existing products could indicate the quality

729 of maps. In areas of low inconsistency, the overall accuracy gap between the GLC-2015 map and

730 previous ones was as small as 0.1%-0.6%. However, for areas of moderate and high inconsistency, the

731 comparison accuracy gap expanded to 19.3%-28.0% and 27.5%-29.7%, respectively. It proved the

732 outperformance of the GLC-2015 map over the other three products in the areas of high identification

733 difficulty.

734 **Table 7. Accuracy assessments of the GLC products in three areas.**

	GLC-2015		Globeland30		FROM_GLC		GLC_FCS30	
	OA	Kappa	OA	Kappa	OA	Kappa	OA	Kappa
Areas of low inconsistency	0.951	0.938	0.945	0.929	0.950	0.936	0.951	0.937
Areas of moderate inconsistency	0.760	0.723	0.561	0.498	0.480	0.411	0.567	0.495
Areas of high inconsistency	0.567	0.498	0.292	0.204	0.286	0.198	0.270	0.160

735   We further provided a comparative analysis of three previous GLC products and the GLC-2015 map

736 in areas of high inconsistency. We calculated the area of pixels with a value equal to 1 in 4° × 4° grids.

737 The grids that the area of pixels with a value equal to 1 account for more than 20% of the total area was

738 selected as grids of high inconsistency. Finally, a total number of 147 grids were selected (Figure 13). To

739 compare the accuracy of the GLC-2015 map and other ones, we utilized scatter plots to represent the

740 relationship between the overall accuracy of one previous product and the GLC-2015 map in each grid

741 of high inconsistency based on the global point-based samples (Figure 13). Most of the points were above

742 the 1:1line, namely the values of y-axes corresponding to those points were larger than the values of x-

743 axes, which demonstrated that the GLC-2015 map performed better than other GLC products in most

744 grids of high inconsistency. It can be found that the fitting line in each scatter plot had the intercept

745 exceeding 0.40, the slope less than 0.55, and the R^2 less than 0.35, showing that the GLC-2015 map had

746 a large difference with other ones.
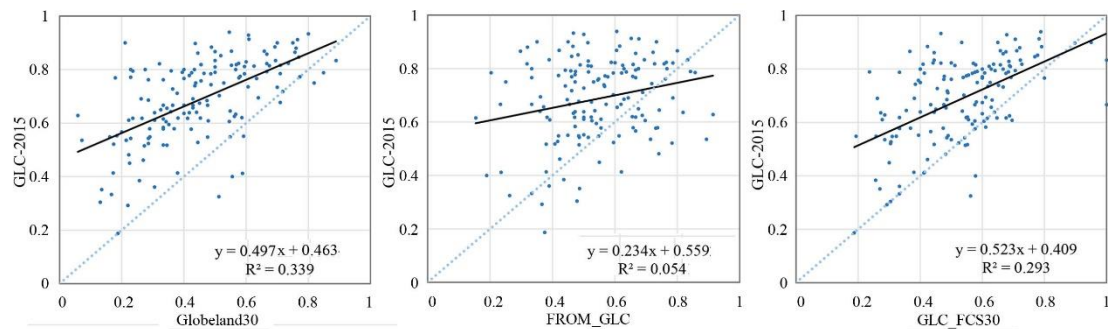
747

748 **Figure 13. Overall accuracy relationship between the GLC-2015 map and other products in grids of high**

749 **inconsistency.**

750   To intuitively compare the mapping result of the GLC-2015 map and three existing ones in areas of

751 high inconsistency, we focused on visual inspection in various areas based on four 5 km×5km patch-

752 based samples and conducted accuracy statistics, as shown in Figure 14. In the detailed display, it is

753 apparent that three previous products had a large difference in four areas. As can be seen from the four

754 visual cases, the typical confusions between LC classes in areas of high inconsistency were as follows:

755 (1) shrubland was easily misclassified as forest and grassland; (2) cropland, grassland, and shrubland

756 were heavily confused with each other; (3) bare land was likely to be mixed with shrubland and grassland.

757 Overall, the GLC-2015 map surpassed other products in the local accuracy assessment. In Western

758 Australian mulga shrublands (Figure 14a), the GLC-2015 map and GLC_FCS30 showed similar spatial

759 distribution and shape of bare land and forest, which was consistent with the real landscape. While the

760 Globeland30 classified bare land as grassland and the FROM_GLC under-classified bare land. As for

761   Zambezian and mopane woodlands (Figure 14b), the GLC-2015 map performed best with OA reaching

762   82.6%, followed by the FROM_GLC. In contrast, other products mixed shrubland with forest or

763   grassland. In agricultural land of Western United States (Figure 14c), the GLC-2015 and Globeland30

764   exhibited similar mapping results with the ground truth while the FROM_GLC had large difference with

765   other products. When it comes to Guinean forest-savanna mosaic (Figure 14d), the GLC-2015 map and

766   Globeland30 showed high spatial consistency, and both had accurate classification profile for cropland,

767   forest, and impervious surfaces, while other products misidentified cropland as other LC classes.
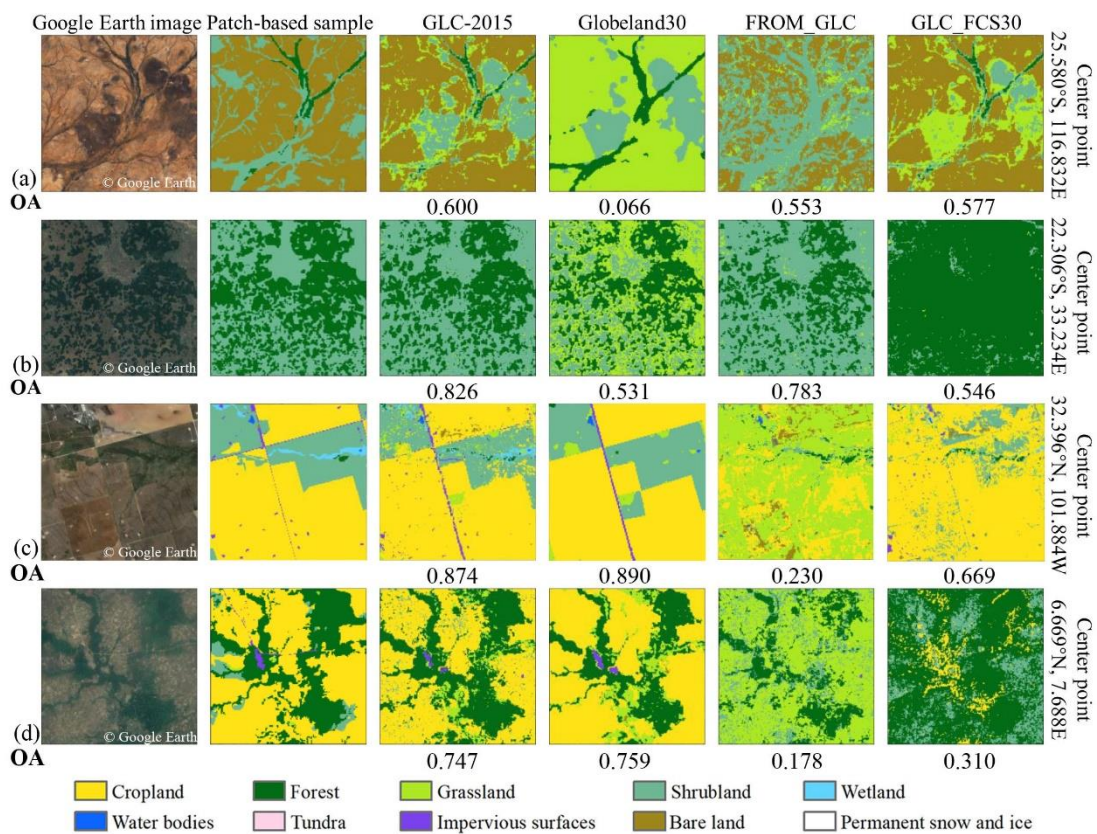
768

769   **Figure 14. Visual comparison between the GLC-2015 map and three other products based on 5km × 5km**

770   **patch-based samples and Google Earth images for four areas of high inconsistency (a-d). The OA for each**

771   **product was calculated by the corresponding patch-based sample.**

772   **4.6 Comparison between DSET and other methods**

773   **4.6.1 Inter-comparison with other data fusion methods**

774   The accuracy assessments on GLC-2015 obtained by DSET and global mapping results from two other

775   data fusion methods were conducted based on two global validation sample sets. The confusion matrixes

776   with the global point-based samples are shown in Table S9 and S10. The OA of the global land cover

777 classification obtained by the MV and SC was 72.1% and 71.8%, respectively. As shown in Table 3, the

778 OA of the GLC-2015 map obtained by the DSET method was 79.5%, which had an improvement of 7.4%

779 and 7.7% compared to mapping results from the MV and SC. In addition, the GLC-2015 map obtained

780 higher PA and UA for most LC classes.

781   When evaluating GLC maps obtained by different data fusion approaches using the global patch-

782 based samples, the DSET method obtained the highest OA of 83.6% and kappa coefficient of 0.566,

783 compared with 80.1% and 0.497 for MV, and 71.8% and 0.391 for SC (Table S11). Here, the DSET

784 method achieved an accuracy improvement of 3.5% and 11.8%. Compared to the two other methods, the

785 DSET improved the accuracy for nearly all the LC classes, especially for grassland, shrubland, and

786 wetland. We also compared the overall accuracy relationship between the DSET and other methods. From

787 the scatter plots (Figure 15), we found that the majority of points were above the 1:1 line, implying DSET

788 had better mapping performance than others in most regions across the globe.
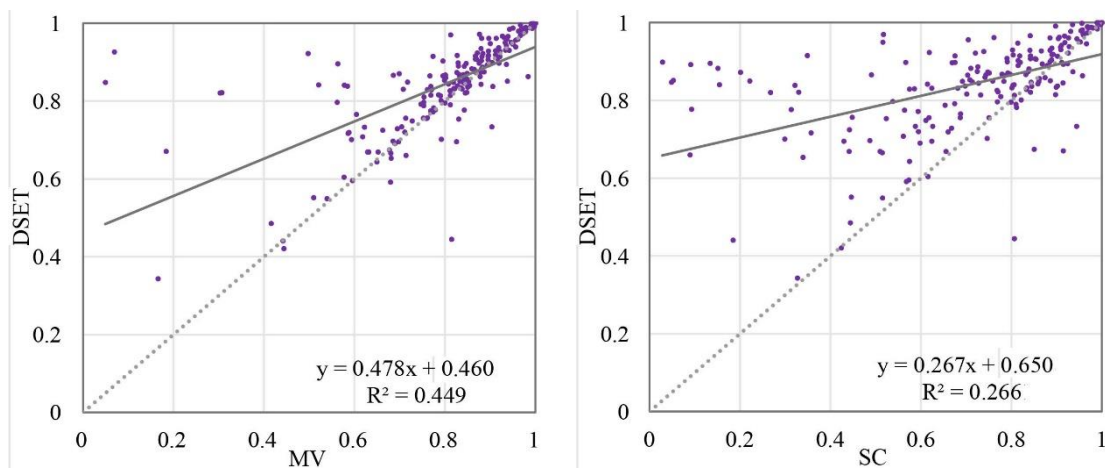
789
790 **Figure 15. Scatter plots between the DSET and other data fusion methods based on the global patch-based**

791 **samples.**

792   Land cover mapping results from the DSET and other methods were also visually illustrated in six

793 tiles with size of the 0.25° covering different continents, as displayed in Figure S14. Despite that mapping

794 results from the DSET and MV depicted similar spatial distribution of LC classes in all tiles except the

795 tile in North America, the DSET more accurately delineated the impervious surfaces of small size which

796 scattered in cropland-dominated (Figure S14a) or arid areas (Figure S14c). Notably, the mapping results

797 from the SC method presented significant differences from that obtained by the DSET and MV. For

798 example, the SC method failed to capture scattered rural residential areas (Figure S14b) and misclassified

799 grassland as cropland (Figure S14d). Overall, the DSET method possessed better recognition

800   performance in various LC classes than the other two methods.

801   **4.6.2 Inter-comparison with the Random Forest**

802   Based on the validation data from 20% of the global point-based samples, we evaluated the quality of

803   the GLC-2015 map obtained by the DSET method and mapping results classified by the RF classifier for

804   a total of 300 grids. The DSET method obtained a mean OA of 80.9% across six continents, while the

805   RF achieved a lower accuracy of 69.9%. From the scatter plots which compared the OA and kappa

806   coefficient between the DSET and RF grid by grid, it was found that the DSET possessed higher accuracy

807   in most grids (Figure S15). Especially, the points were clustered in the upper right corner of the plot

808   (Figure S15a), which indicated that the RF classifier trained with the global point-based samples

809   performed well in those selected grids though it was inferior to the DSET method. Figure S16 shows the

810   OA of the DSET and RF across six continents. We found that the DSET method outperformed RF

811   classifier for each continent. Especially, the mapping results of both two methods presented the lowest

812   accuracy in Oceania. It may be because the selected grids are located in regions with heterogeneous

813   landscape. As for the box plot for the RF classifier, the low hinge exceeded 60.00% in all continents

814   except Oceania, demonstrating the reliability of the RF classifier trained by the global point-based

815   samples. Nevertheless, the performance of the RF classifier was worse than the DSET method. This

816   highlights the feasibility of the DSET method in integrating the existing maps for a better one.

817   **4.7 Advancement and Limitations**

818   To address the problem that current 30m GLC products have great inconsistency in heterogeneous

819   areas and low mapping accuracy for spectral similar LC classes, this study adopted a multi-source

820   product fusion approach based on DSET to create an improved global land cover map (GLC-2015). The

821   results show that the GLC-2015 had good mapping performance with OA reaching 79.5% and 83.6%

822   based on two different validation sets. Compared with those existing products, the GLC-2015 greatly

823   improved the accuracy across the globe, especially in areas of high inconsistency with a significant

824   improvement of 27.5%-29.7%. Compared with other commonly used data fusion methods, the adopted

825   DSET approach provided higher OA and kappa coefficient which showed the benefit of the DEST in

826   integrating various land cover data. No matter from the respective of the global point-based samples or

827   the global patch-based samples, the GLC-2015 showed relatively low accuracy for grassland, shrubland,

828 and wetland compared to other LC classes. Those LC classes are challenging to map at the global scale

829 duo to their spectral similarity to other classes, ambiguous definitions, or variety with regions. However,

830 compared to other existing 30m GLC products, the GLC-2015 map performed better with the PA and OA

831 ranking first or second for grassland, shrubland, and wetland, which indicated the improvement of the

832 GLC-2015 in poorly-mapped LC classes. It was found that the GLC-2015 map had worse performance

833 in areas with more disagreements (Table 7). However, the GLC-2015 map surpassed other products in

834 the areas with different agree of inconsistency. Moreover, the accuracy gap between the GLC-2015 map

835 and other ones in areas of high inconsistency was larger than that in areas with fewer disagreements,

836 implying that the GLC-2015 map provides a more accurate characterization of land cover in poorly-

837 mapped areas. Although the GLC-2015 map was not capable of avoiding all the wrong mapping results

838 caused by the disagreements from the candidate GLC products, it outperformed the existing products

839 from the aspects of mapping accuracy for the easily misclassified classes and areas with great

840 inconsistency.

841   Although the GLC-2015 map can evidently improve mapping accuracy in inconsistent areas, there

842 are still some uncertainties. First, we used three multiple-class GLC maps and four single-class GLC

843 maps as the source data for integration. Since those products provided information of land cover at the

844 global scale, classification errors inevitably exist in some specific regions. The multisource product

845 fusion method based on DEST depends highly on the quality of those candidate maps such that the

846 inconsistency between those source maps might lead to incorrect classification. Second, the date time of

847 the GlobeLand30 is different from that of other maps. Because of the five-year time interval, there are

848 changes in land cover, which inevitably distort the fusion results. However, the changed areas are tiny

849 compared to the world's terrestrial area. The uncertainties caused by the LC changes are minor than those

850 from classification errors. In addition, the global point-based samples were used to evaluate the reliability

851 of each product. The accuracy of GlobeLand30 was lower than the other products for areas with LC

852 changes. In this case, the fusion depended more on other maps to avoid the errors caused by LC changes.

853 Third, due to the different LC definitions, uncertainties in classification system conversion are inevitable

854 (Zhang et al., 2017), which might cause problems for the fusion based on the DSET method. However,

855 we conducted a reliability evaluation of the candidate maps to reduce the influence of uncertainties in

856 classification system conversion on the fusion. The point-based samples used for reliability evaluation

857 were labeled referring to the LC definitions in our classification system so that all the maps were

858 evaluated under the criterion of the classification system we used. By the reliability evaluation, the

859 candidate maps were assessed to have lower accuracy for areas with mismatched information. When

860 integrating all the maps grid by grid, the mismatched information would contribute less to the fusion.

861 Lastly, most candidate LC products used a simple classification system without a level-2 classification

862 system, so they made no contributions to a more detailed classification system when they served as source

863 data for data fusion. Although some maps provided detailed LC classification results, such as the

864 GLC_FCS30 and FROM_GLC for 2015, there might be several challenges in the standardization and

865 uniformity of level-2 classification systems due to the large discrepancies in the definition and criteria.

866 Therefore, the GLC-2015 adopted a simple classification system containing 10 major LC classes. In

867 future work, measures will be taken to meet the expectation of a more detailed classification system for

868 GLC mapping. An improved GLC product with a detailed classification system rather than a simple one-

869 level classification system can be further developed based on the highly applicable and general DSET

870 method whenever more products with diverse LC classes are available. Additionally, a feasible

871 framework for the conversion of different level-2 classification systems into a uniform system should be

872 developed.

873 **5. Data availability**

874 The improved global land cover map in 2015 with 30 m resolution is available at

875 https://doi.org/10.6084/m9.figshare.22358143.v2 (Li et al., 2022). The GLC-2015 product is organized

876 by a total of 1507 4° × 4° geographical grids in GeoTIFF format across the world's terrestrial area. Each

877 image of the GLC-2015 product is named as "GLC-2015_lon_lat" (lon and lat represent the longitude

878 and latitude and of the grid's lower left corner, respectively).

879 **6. Conclusions**

880 GLC information at fine spatial resolution is vital for the global environment and climate studies which

881 can capture the footprint of human activity. Resulting from the differences in classification scheme,

882 satellite sensor data, classification algorithms and sampling strategies, the existing GLC products have

883 high inconsistency in some parts of the world, especially in fragmented areas and transition zones. More

accurate and reliable data with accuracy improved in areas of high mapping inconsistency is very desirable. In this study, with the help of the GEE platform, we developed the GLC-2015 map by integrating multiple existing GLC maps based on the DSET. The GLC-2015 map can significantly increase the mapping accuracy and possess good recognition performance in various LC classes.

The GLC-2015 map was validated by both the global point-based samples and the global patch-based samples. Accuracy assessments show that the GLC-2015 map achieved an OA of 79.5%, a kappa coefficient of 0.757 using a total of 34,117 global point-based samples, and an OA of 83.6%, a kappa coefficient of 0.566 using a total of 201 global patch-based samples. Data inter-comparison indicated that the GLC-2015 map surpassed other three products both visually and quantitatively, by OA improvement of 14.0%-17.8% validated with the global point-based samples and 5.9%-24.5% with the global patch-based samples. Compared to other products, there are fewer misclassifications in the GLC-2015 map for most LC classes, such as forest, cropland, shrubland, and water bodies. Meanwhile, the GLC-2015 map outperformed others in terms of OA and kappa coefficient across different ecoregions and different continents. Notably, the GLC-2015 map showed better performance than others by an increment of 0.1%-0.6%. in overall accuracy for areas of low inconsistency, 19.3%-28.0% for areas of moderate inconsistency, and 27.5%-29.7% for areas of high inconsistency. In addition, the mapping results obtained by the DSET surpassed other data fusion methods with OA improvement of 7.4%-7.7% via the global point-based samples and 3.5%-11.8% via the global patch-based samples. Therefore, it can be concluded that the GLC-2015 map is a robust and reliable map that can significantly improve mapping accuracy compared to previous GLC products and mapping results from other common data fusion methods.

Author contributions

XL and XX conceived the research. BL and XX designed and carried out the experiments. QS and DH provided data. BL wrote the original manuscript. XX, HZ and YC reviewed the writing.

Competing interests

The authors declare that they have no conflict of interest.

Financial support

This research has been supported by the National Key Research & Development Program of China (Grant No. 2019YFA0607203), the National Natural Science Foundation of China (Grant No. 42001326, 42171409), and the Natural Science Foundation of Guangdong Province of China (Grant No. 2022A1515012207).

References

Ban, Y., Gong, P., and Giri, C.: Global land cover mapping using Earth observation satellite data: Recent progresses and challenges, ISPRS J. Photogramm., 103, 1-6, https://doi.org/10.1016/j.isprsjprs.2015.01.001, 2015.

Bartholomé, E. and Belward, A. S.: GLC2000: A new approach to global land cover mapping from Earth observation data, Int. J. Remote Sens., 26, 1959-1977, https://doi.org/10.1080/01431160412331291297, 2005.

Bounoua, L., DeFries, R., Collatz, G. J., Sellers, P., and Khan, H.: Effects of land cover conversion on surface climate, Clim. Change, 52, 29-64, https://doi.org/10.1023/A:1013051420309, 2002.

Bunting, P., Rosenqvist, A., Lucas, R. M., Rebelo, L. M., Hilarides, L., Thomas, N., Hardy, A., Itoh, T., Shimada, M., and Finlayson, C. M.: The Global Mangrove Watch—A new 2010 global baseline of mangrove extent, Remote Sensing, 10, https://doi.org/10.3390/rs10101669, 2018.

Chapin, F. S. I., Zavaleta, E. S., Eviner, V. T., Naylor, R. L., Vitousek, P. M., Reynolds, H. L., Hooper, D. U., Lavorel, S., Sala, O. E., Hobbie, S. E., Mack, M. C., and Díaz, S.: Consequences of changing biodiversity, Nature, 405, 234-242, https://doi.org/10.1038/35012241, 2000.

Chen, J., Chen, J., Liao, A., Cao, X., Chen, L., Chen, X., He, C., Han, G., Peng, S., Lu, M., Zhang, W., Tong, X., and Mills, J.: Global land cover mapping at 30m resolution: A POK-based operational approach, ISPRS J. Photogramm., 103, 7-27, https://doi.org/10.1016/j.isprsjprs.2014.09.002, 2015.

Chen, T. M. and Venkataramanan, V.: Dempster-Shafer theory for intrusion detection in ad hoc networks, IEEE Internet comput., 9, 35-41, https://doi.org/10.1109/MIC.2005.123, 2005.

Clinton, N., Yu, L., and Gong, P.: Geographic stacking: Decision fusion to increase global land cover map accuracy, ISPRS J. Photogramm., 103, 57-65, https://doi.org/10.1016/j.isprsjprs.2015.02.010, 2015.

Land Cover CCI: Product User Guide Version 2: https://www.esa-landcover-cci.org/?q=webfm_send/84, last access: 21 January 2022.

DeFries, R. S., Houghton, R. A., Hansen, M. C., Field, C. B., Skole, D., and Townshend, J.: Carbon emissions from tropical deforestation and regrowth based on satellite observations for the 1980s and 1990s, Proc. Natl. Acad. Sci. U.S.A., 99, 14256, https://doi.org/10.1073/pnas.182560099, 2002.

Foley, J. A., DeFries, R., Asner, G. P., Barford, C., Bonan, G., Carpenter, S. R., Chapin, F. S., Coe, M. T., Daily, G. C., Gibbs, H. K., Helkowski, J. H., Holloway, T., Howard, E. A., Kucharik, C. J., Monfreda, C., Patz, J. A., Prentice, I. C., Ramankutty, N., and Snyder, P. K.: Global Consequences of Land Use, Science, 309, 570-574, https://doi.org/10.1126/science.1111772, 2005.

Friedl, M. A., Sulla-Menashe, D., Tan, B., Schneider, A., Ramankutty, N., Sibley, A., and Huang, X.: MODIS Collection 5 global land cover: Algorithm refinements and characterization of new datasets,

Remote Sens. Environ., 114, 168-182, https://doi.org/10.1016/j.rse.2009.08.016, 2010.

Fritz, S., You, L., Bun, A., See, L., McCallum, I., Schill, C., Perger, C., Liu, J., Hansen, M., and Obersteiner, M.: Cropland for sub-Saharan Africa: A synergistic approach using five land cover data sets, Geophy. Res. Lett., 38, L04404, https://doi.org/10.1029/2010GL046213, 2011.

Gao, Y., Liu, L., Zhang, X., Chen, X., Mi, J., and Xie, S.: Consistency analysis and accuracy assessment of three global 30 m land-cover products over the European Union using the LUCAS dataset, Remote Sensing, 12, 3479, https://doi.org/10.3390/rs12213479, 2020.

Gengler, S. and Bogaert, P.: Combining land cover products using a minimum divergence and a Bayesian data fusion approach, Int. J. Geogr. Inf. Sci., 32, 806-826, https://doi.org/10.1080/13658816.2017.1413577, 2018.

Giri, C., Zhu, Z., and Reed, B.: A comparative analysis of the Global Land Cover 2000 and MODIS land cover datasets, Remote Sens. Environ., 94, 123-132, https://doi.org/10.1016/j.rse.2004.09.005, 2005.

Giri, C., Pengra, B., Long, J., and Loveland, T. R.: Next generation of global land cover characterization, mapping, and monitoring, Int. J. Appl. Earth Observ., 25, 30-37, https://doi.org/10.1016/j.jag.2013.03.005, 2013.

Gómez, C., White, J. C., and Wulder, M. A.: Optical remotely sensed time series data for land cover classification: A review, ISPRS J. Photogramm., 116, 55-72, https://doi.org/10.1016/j.isprsjprs.2016.03.008, 2016.

Gong, P.: Remote sensing of environmental change over China: A review, Sci. Bull., 57, 2793-2801, https://doi.org/10.1007/s11434-012-5268-y, 2012.

Gong, P., Yu, L., Li, C., Wang, J., Liang, L., Li, X., Ji, L., Bai, Y., Cheng, Y., and Zhu, Z.: A new research paradigm for global land cover mapping, Ann. GIS, 22, 87-102, https://doi.org/10.1080/19475683.2016.1164247, 2016.

Gong, P., Li, X., Wang, J., Bai, Y., Chen, B., Hu, T., Liu, X., Xu, B., Yang, J., Zhang, W., and Zhou, Y.: Annual maps of global artificial impervious area (GAIA) between 1985 and 2018, Remote Sens. Environ., 236, 111510, https://doi.org/10.1016/j.rse.2019.111510, 2020.

Gong, P., Wang, J., Yu, L., Zhao, Y., Zhao, Y., Liang, L., Niu, Z., Huang, X., Fu, H., Liu, S., Li, C., Li, X., Fu, W., Liu, C., Xu, Y., Wang, X., Cheng, Q., Hu, L., Yao, W., Zhang, H., Zhu, P., Zhao, Z., Zhang, H., Zheng, Y., Ji, L., Zhang, Y., Chen, H., Yan, A., Guo, J., Yu, L., Wang, L., Liu, X., Shi, T., Zhu, M., Chen, Y., Yang, G., Tang, P., Xu, B., Giri, C., Clinton, N., Zhu, Z., Chen, J., and Chen, J.: Finer resolution observation and monitoring of global land cover: first mapping results with Landsat TM and ETM+ data, Int. J. Remote Sens., 34, 2607-2654, https://doi.org/10.1080/01431161.2012.748992, 2013.

Grekousis, G., Mountrakis, G., and Kavouras, M.: An overview of 21 global and 43 regional land-cover mapping products, Int. J. Remote Sens., 36, 5309-5335, https://doi.org/10.1080/01431161.2015.1093195, 2015.

Grimm, N. B., Faeth, S. H., Golubiewski, N. E., Redman, C. L., Wu, J., Bai, X., and Briggs, J. M.: Global change and the ecology of cities, Science, 319, 756-760, https://doi.org/10.1126/science.1150195, 2008.

Hansen, M. C., Defries, R. S., Townshend, J. R. G., and Sohlberg, R.: Global land cover classification at 1 km spatial resolution using a classification tree approach, Int. J. Remote Sens., 21, 1331-1364, https://doi.org/10.1080/014311600210209, 2000.

Hansen, M. C., Potapov, P. V., Moore, R., Hancher, M., Turubanova, S. A., Tyukavina, A., Thau, D., Stehman, S. V., Goetz, S. J., Loveland, T. R., Kommareddy, A., Egorov, A., Chini, L., Justice, C. O.,

and Townshend, J. R. G.: High-resolution global maps of 21st-century forest cover change, Science, 342, 850-853, https://doi.org/10.1126/science.1244693, 2013.

Herold, M., Mayaux, P., Woodcock, C. E., Baccini, A., and Schmullius, C.: Some challenges in global land cover mapping: An assessment of agreement and accuracy in existing 1 km datasets, Remote Sens. Environ., 112, 2538-2556, https://doi.org/10.1016/j.rse.2007.11.013, 2008.

Hu, L., Chen, Y., Xu, Y., Zhao, Y., Yu, L., Wang, J., and Gong, P.: A 30 meter land cover mapping of China with an efficient clustering algorithm CBEST, Science China Earth Sciences, 57, 2293-2304, https://doi.org/10.1007/s11430-014-4917-1, 2014.

Hu, S., Niu, Z., Chen, Y., Li, L., and Zhang, H.: Global wetlands: Potential distribution, wetland loss, and status, Sci. Total Environ., 586, 319-327, https://doi.org/10.1016/j.scitotenv.2017.02.001, 2017.

Huang, X., Yang, J., Wang, W., and Liu, Z.: Mapping 10 m global impervious surface area (GISA-10m) using multi-source geospatial data, Earth Syst. Sci. Data, 14, 3649-3672, https://essd.copernicus.org/articles/14/3649/2022/, 2022.

Huang, X., Li, J., Yang, J., Zhang, Z., Li, D., and Liu, X.: 30 m global impervious surface area dynamics and urban expansion pattern observed by Landsat satellites: From 1972 to 2019, Science China Earth Sciences, 64, 1922-1933, https://10.1007/s11430-020-9797-9, 2021.

Iwao, K., Nasahara, K. N., Kinoshita, T., Yamagata, Y., Patton, D., and Tsuchida, S.: Creation of new global land cover map with map integration, J. Geogr. Inf. Syst., 3, 160-165, https://doi.org/10.4236/jgis.2011.32013, 2011.

Jin, Q., Xu, E., and Zhang, X.: A fusion method for multisource land cover products based on superpixels and statistical extraction for enhancing resolution and improving accuracy, Remote Sensing, 14, 1676, https://doi.org/10.3390/rs14071676, 2022.

Jung, M., Henkel, K., Herold, M., and Churkina, G.: Exploiting synergies of global land cover products for carbon cycle modeling, Remote Sens. Environ., 101, 534-553, https://doi.org/10.1016/j.rse.2006.01.020, 2006.

Kang, J., Wang, Z., Sui, L., Yang, X., Ma, Y., and Wang, J.: Consistency analysis of remote sensing land cover products in the tropical rainforest climate region: A case study of Indonesia, Remote Sensing, 12, 1410, https://doi.org/10.3390/rs12091410, 2020.

Kim, D., Lim, C.-H., Song, C., Lee, W.-K., Piao, D., Heo, S., and Jeon, S.: Estimation of future carbon budget with climate change and reforestation scenario in North Korea, Adv. Space Res., 58, 1002-1016, https://doi.org/10.1016/j.asr.2016.05.049, 2016.

Li, B., Xu, X., Liu, X., Shi, Q., Zhuang, H., Cai, Y., and He, D.: An improved global land cover mapping in 2015 with 30 m resolution (GLC-2015) based on a multi-source product fusion approach. [dataset], https://doi.org/10.6084/m9.figshare.22358143.v2, 2022.

Li, C., Gong, P., Wang, J., Zhu, Z., Biging, G. S., Yuan, C., Hu, T., Zhang, H., Wang, Q., Li, X., Liu, X., Xu, Y., Guo, J., Liu, C., Hackman, K. O., Zhang, M., Cheng, Y., Yu, L., Yang, J., Huang, H., and Clinton, N.: The first all-season sample set for mapping global land cover with Landsat-8 data, Sci. Bull., 62, 508-515, https://doi.org/10.1016/j.scib.2017.03.011, 2017.

Liao, A., Chen, L., Chen, J., He, C., Cao, X., Chen, J., Peng, S., Sun, F., and Gong, P.: High-resolution remote sensing mapping of global land water, Science China Earth Sciences, 57, 2305-2316, https://doi.org/10.1007/s11430-014-4918-0, 2014.

Liu, H., Gong, P., Wang, J., Clinton, N., Bai, Y., and Liang, S.: Annual dynamics of global land cover and its long-term changes from 1982 to 2015, Earth Syst. Sci. Data, 12, 1217-1243, https://doi.org/10.5194/essd-12-1217-2020, 2020a.

Liu, H., Gong, P., Wang, J., Wang, X., Ning, G., and Xu, B.: Production of global daily seamless data cubes and quantification of global land cover change from 1985 to 2020 - iMap World 1.0, Remote Sens. Environ., 258, 112364, https://doi.org/10.1016/j.rse.2021.112364, 2021a.

Liu, J., Kuang, W., Zhang, Z., Xu, X., Qin, Y., Ning, J., Zhou, W., Zhang, S., Li, R., Yan, C., Wu, S., Shi, X., Jiang, N., Yu, D., Pan, X., and Chi, W.: Spatiotemporal characteristics, patterns and causes of land use changes in China since the late 1980s, Dili Xuebao/Acta Geogr. Sin., 69, 3-14, https://doi.org/10.11821/dlxb201401001, 2014.

Liu, K. and Xu, E.: Fusion and correction of multi-source land cover products based on spatial detection and uncertainty reasoning methods in Central Asia, Remote Sensing, 13, 244, https://doi.org/10.3390/rs13020244, 2021.

Liu, L., Zhang, X., Gao, Y., Chen, X., Shuai, X., and Mi, J.: Finer-resolution mapping of global land cover: Recent developments, consistency analysis, and prospects, Journal of Remote Sensing, 2021, 5289697, https://doi.org/10.34133/2021/5289697, 2021b.

Liu, X., Huang, Y., Xu, X., Li, X., Li, X., Ciais, P., Lin, P., Gong, K., Ziegler, A. D., and Chen, A.: High-spatiotemporal-resolution mapping of global urban change from 1985 to 2015, Nature Sustainability, 3, 564-570, 2020b.

Liu, X., Huang, Y., Xu, X., Li, X., Li, X., Ciais, P., Lin, P., Gong, K., Ziegler, A. D., Chen, A., Gong, P., Chen, J., Hu, G., Chen, Y., Wang, S., Wu, Q., Huang, K., Estes, L., and Zeng, Z.: High-spatiotemporal-resolution mapping of global urban change from 1985 to 2015, Nature Sustainability, 3, 564-570, https://doi.org/10.1038/s41893-020-0521-x, 2020c.

Loveland, T. R., Reed, B. C., Brown, J. F., Ohlen, D. O., Zhu, Z., Yang, L., and Merchant, J. W.: Development of a global land cover characteristics database and IGBP DISCover from 1 km AVHRR data, Int. J. Remote Sens., 21, 1303-1330, https://doi.org/10.1080/014311600210191, 2000.

Lu, M., Wu, W., You, L., See, L., Fritz, S., Yu, Q., Wei, Y., Chen, D., Yang, P., and Xue, B.: A cultivated planet in 2010 – Part 1: The global synergy cropland map, Earth Syst. Sci. Data, 12, 1913-1928, https://essd.copernicus.org/articles/12/1913/2020/, 2020.

Ludwig, C., Walli, A., Schleicher, C., Weichselbaum, J., and Riffler, M.: A highly automated algorithm for wetland detection using multi-temporal optical satellite data, Remote Sens. Environ., 224, 333-351, https://doi.org/10.1016/j.rse.2019.01.017, 2019.

Mayaux, P., Bartholomé, E., Fritz, S., and Belward, A.: A new land-cover map of Africa for the year 2000, J. Biogeogr., 31, 861-877, https://doi.org/10.1111/j.1365-2699.2004.01073.x, 2004.

McCallum, I., Obersteiner, M., Nilsson, S., and Shvidenko, A.: A spatial comparison of four satellite derived 1km global land cover datasets, Int. J. Appl. Earth Observ., 8, 246-255, https://doi.org/10.1016/j.jag.2005.12.002, 2006.

Meng, Z., Dong, J., Ellis, E. C., Metternicht, G., Qin, Y., Song, X.-P., Löfqvist, S., Garrett, R. D., Jia, X., and Xiao, X.: Post-2020 biodiversity framework challenged by cropland expansion in protected areas, Nature Sustainability, https://doi.org/10.1038/s41893-023-01093-w, 2023.

Meyer, M. F., Labou, S. G., Cramer, A. N., Brousil, M. R., and Luff, B. T.: The global lake area, climate, and population dataset, Sci. Data, 7, 174, https://doi.org/10.1038/s41597-020-0517-4, 2020.

Moody, A. and Woodcock, C.: Scale-dependent errors in the estimation of land-cover proportions: Implications for global land-cover datasets, Photogramm. Eng. Remote Sens., 60, 585-594, 1994.

Pekel, J. F., Cottam, A., Gorelick, N., and Belward, A. S.: High-resolution mapping of global surface water and its long-term changes, Nature, 540, 418-422, https://doi.org/10.1038/nature20584, 2016.

Pengra, B. W., Stehman, S. V., Horton, J. A., Dockter, D. J., Schroeder, T. A., Yang, Z., Cohen, W. B.,

1081 Healey, S. P., and Loveland, T. R.: Quality control and assessment of interpreter consistency of annual
1082 land cover reference data in an operational national monitoring program, Remote Sens. Environ., 238,
1083 111261, https://doi.org/10.1016/j.rse.2019.111261, 2020.

1084 Pickens, A. H., Hansen, M. C., Hancher, M., Stehman, S. V., Tyukavina, A., Potapov, P., Marroquin, B.,
1085 and Sherani, Z.: Mapping and sampling to characterize global inland water dynamics from 1999 to
1086 2018 with full Landsat time-series, Remote Sens. Environ., 243, 111792,
1087 https://doi.org/10.1016/j.rse.2020.111792, 2020.

1088 Razi, S., Karami Mollaei, M. R., and Ghasemi, J.: A novel method for classification of BCI multi-class
1089 motor imagery task based on Dempster–Shafer theory, Inf. Sci., 484, 14-26,
1090 https://doi.org/10.1016/j.ins.2019.01.053, 2019.

1091 Rottensteiner, F., Trinder, J. C., Clode, S., and Kubik, K.: Using the Dempster-Shafer method for the
1092 fusion of LIDAR data and multi-spectral images for building detection, Inform. Fusion., 6, 283-300,
1093 https://doi.org/10.1016/j.inffus.2004.06.004, 2005.

1094 Running, S. W.: Ecosystem disturbance, carbon, and climate, Science, 321, 652-653,
1095 https://doi.org/10.1126/science.1159607, 2008.

1096 Schewe, J., Gosling, S. N., Reyer, C., Zhao, F., Ciais, P., Elliott, J., Francois, L., Huber, V., Lotze, H. K.,
1097 Seneviratne, S. I., van Vliet, M. T. H., Vautard, R., Wada, Y., Breuer, L., Büchner, M., Carozza, D. A.,
1098 Chang, J., Coll, M., Deryng, D., de Wit, A., Eddy, T. D., Folberth, C., Frieler, K., Friend, A. D., Gerten,
1099 D., Gudmundsson, L., Hanasaki, N., Ito, A., Khabarov, N., Kim, H., Lawrence, P., Morfopoulos, C.,
1100 Müller, C., Müller Schmied, H., Orth, R., Ostberg, S., Pokhrel, Y., Pugh, T. A. M., Sakurai, G., Satoh,
1101 Y., Schmid, E., Stacke, T., Steenbeek, J., Steinkamp, J., Tang, Q., Tian, H., Tittensor, D. P., Volkholz,
1102 J., Wang, X., and Warszawski, L.: State-of-the-art global models underestimate impacts from climate
1103 extremes, Nat. Commun., 10, 1005, https://doi.org/10.1038/s41467-019-08745-6, 2019.

1104 See, L., Schepaschenko, D., Lesiv, M., McCallum, I., Fritz, S., Comber, A., Perger, C., Schill, C., Zhao,
1105 Y., Maus, V., Siraj, M. A., Albrecht, F., Cipriani, A., Vakolyuk, M. y., Garcia, A., Rabia, A. H., Singha,
1106 K., Marcarini, A. A., Kattenborn, T., Hazarika, R., Schepaschenko, M., van der Velde, M., Kraxner, F.,
1107 and Obersteiner, M.: Building a hybrid land cover map with crowdsourcing and geographically
1108 weighted regression, ISPRS J. Photogramm., 103, 48-56,
1109 https://doi.org/10.1016/j.isprsjprs.2014.06.016, 2015.

1110 Shafizadeh-Moghadam, H., Minaei, M., Feng, Y., and Pontius, R. G.: GlobeLand30 maps show four
1111 times larger gross than net land change from 2000 to 2010 in Asia, Int. J. Appl. Earth Observ., 78, 240-
1112 248, https://doi.org/10.1016/j.jag.2019.01.003, 2019.

1113 Shimada, M., Itoh, T., Motooka, T., Watanabe, M., Shiraishi, T., Thapa, R., and Lucas, R.: New global
1114 forest/non-forest maps from ALOS PALSAR data (2007–2010), Remote Sens. Environ., 155, 13-31,
1115 https://doi.org/10.1016/j.rse.2014.04.014, 2014.

1116 Song, X., Hansen, M. C., Stehman, S. V., Potapov, P. V., Tyukavina, A., Vermote, E. F., and Townshend,
1117 J. R.: Global land change from 1982 to 2016, Nature, 560, 639-643, https://doi.org/10.1038/s41586-018-
1118 0411-9, 2018.

1119 Sun, B., Chen, X., and Zhou, Q.: Uncertainty assessment of GlobeLand30 land cover data set over central
1120 Asia, Int. Arch. Photogramm. Remote Sens. Spat. Inf. Sci., 41, 1313, https://doi.org/10.5194/isprs-
1121 archives-XLI-B8-1313-2016, 2016.

1122 Teluguntla, P., Thenkabail, P. S., Oliphant, A., Xiong, J., Gumma, M. K., Congalton, R. G., Yadav, K.,
1123 and Huete, A.: A 30-m landsat-derived cropland extent product of Australia and China using random
1124 forest machine learning algorithm on Google Earth Engine cloud computing platform, ISPRS J.

1125   Photogramm., 144, 325-340, https://doi.org/10.1016/j.isprsjprs.2018.07.017, 2018.

1126   Verburg, P. H., Neumann, K., and Nol, L.: Challenges in using land use and land cover data for global
1127   change studies, Glob. Change Biol., 17, 974-989, https://doi.org/10.1111/j.1365-2486.2010.02307.x,
1128   2011.

1129   Verburg, P. H., Mertz, O., Erb, K.-H., Haberl, H., and Wu, W.: Land system change and food security:
1130   towards multi-scale land system solutions, Curr. Opin. Environ. Sustain., 5, 494-502,
1131   https://doi.org/10.1016/j.cosust.2013.07.003, 2013.

1132   Wickham, J., Stehman, S. V., Sorenson, D. G., Gass, L., and Dewitz, J. A.: Thematic accuracy assessment
1133   of the NLCD 2016 land cover for the conterminous United States, Remote Sens. Environ., 257, 112357,
1134   https://doi.org/10.1016/j.rse.2021.112357, 2021.

1135   Wu, J., Wang, X., Zhong, B., Yang, A., Jue, K., Wu, J., Zhang, L., Xu, W., Wu, S., Zhang, N., and Liu,
1136   Q.: Ecological environment assessment for Greater Mekong Subregion based on Pressure-State-
1137   Response   framework   by   remote   sensing,   Ecol.   Indic.,   117,   106521,
1138   https://doi.org/10.1016/j.ecolind.2020.106521, 2020.

1139   Wulder, M. A., Li, Z., Campbell, E. M., White, J. C., Hobart, G., Hermosilla, T., and Coops, N. C.: A
1140   national assessment of wetland status and trends for Canada's forested ecosystems using 33 years of
1141   earth observation satellite data, Remote Sensing, 10, 1623, https://doi.org/10.3390/rs10101623, 2018.

1142   Xiong, J., Thenkabail, P. S., Tilton, J. C., Gumma, M. K., Teluguntla, P., Oliphant, A., Congalton, R. G.,
1143   Yadav, K., and Gorelick, N.: Nominal 30-m cropland extent map of continental Africa by integrating
1144   pixel-based and object-based algorithms Using Sentinel-2 and Landsat-8 data on Google Earth Engine,
1145   Remote Sensing, 9, 1065, https://doi.org/10.3390/rs9101065, 2017.

1146   Xu, G., Zhang, H., Chen, B., Zhang, H., Yan, J., Chen, J., Che, M., Lin, X., and Dou, X.: A Bayesian
1147   based method to generate a synergetic land-cover map from existing land-cover products., Remote
1148   Sensing, 6, 5589-5613, https://doi.org/10.3390/rs606558910.3390/rs6065589, 2014.

1149   Xue, J., Wang, Y., Teng, H., Wang, N., Li, D., Peng, J., Biswas, A., and Shi, Z.: Dynamics of vegetation
1150   greenness and Iits response to climate change in Xinjiang over the past two decades, Remote Sensing,
1151   13, 4063, https://doi.org/10.3390/rs13204063, 2021.

1152   Yang, J. and Huang, X.: The 30 m annual land cover dataset and its dynamics in China from 1990 to
1153   2019, Earth Syst. Sci. Data, 13, 3907-3925, https://doi.org/10.5194/essd-13-3907-2021, 2021.

1154   Yang, J., Gong, P., Fu, R., Zhang, M., Chen, J., Liang, S., Xu, B., Shi, J., and Dickinson, R.: The role of
1155   satellite   remote   sensing   in   climate   change   studies,   Nat.   Clim.   Chang.,   3,   875-883,
1156   https://doi.org/10.1038/nclimate1908, 2013.

1157   Yang, L., Jin, S., Danielson, P., Homer, C., Gass, L., Bender, S. M., Case, A., Costello, C., Dewitz, J.,
1158   Fry, J., Funk, M., Granneman, B., Liknes, G. C., Rigge, M., and Xian, G.: A new generation of the
1159   United States National Land Cover Database: Requirements, research priorities, design, and
1160   implementation   strategies,   ISPRS   J.   Photogramm.,   146,   108-123,
1161   https://doi.org/10.1016/j.isprsjprs.2018.09.006, 2018.

1162   Yang, Y., Xiao, P., Feng, X., and Li, H.: Accuracy assessment of seven global land cover datasets over
1163   China, ISPRS J. Photogramm., 125, 156-173, https://doi.org/10.1016/j.isprsjprs.2017.01.016, 2017.

1164   Yu, L., Wang, J., Clinton, N., Xin, Q., Zhong, L., Chen, Y., and Gong, P.: FROM-GC: 30 m global
1165   cropland extent derived through multisource data integration, Int. J. Digit. Earth, 6, 521-533,
1166   https://doi.org/10.1080/17538947.2013.822574, 2013.

1167   Zhang, C., Dong, J., and Ge, Q.: Quantifying the accuracies of six 30-m cropland datasets over China: A
1168   comparison   and   evaluation   analysis,   Comput.   Electron.   Agric.,   197,   106946,

1169   https://doi.org/10.1016/j.compag.2022.106946, 2022.

1170 Zhang, M., Ma, M., De Maeyer, P., and Kurban, A.: Uncertainties in classification system conversion

1171   and an analysis of inconsistencies in global land cover products, ISPRS Int. J. Geo Inf., 6, 112,

1172   https://doi.org/10.3390/ijgi6040112, 2017.

1173 Zhang, X., Liu, L., Chen, X., Gao, Y., Xie, S., and Mi, J.: GLC_FCS30: global land-cover product with

1174   fine classification system at 30 m using time-series Landsat imagery, Earth Syst. Sci. Data, 13, 2753-

1175   2776, https://doi.org/10.5194/essd-13-2753-2021, 2021.

1176 Zhang, X., Liu, L., Zhao, T., Chen, X., Lin, S., Wang, J., Mi, J., and Liu, W.: GWL_FCS30: a global 30

1177   m wetland map with a fine classification system using multi-sourced and time-series remote sensing

1178   imagery in 2020, Earth Syst. Sci. Data, 15, 265-293, https://doi.org/10.5194/essd-15-265-2023, 2023.

1179 Zhang, X., Long, T., He, G., Guo, Y., Yin, R., Zhang, Z., Xiao, H., Li, M., and Bo, C.: Rapid generation

1180   of global forest cover map using Landsat based on the forest ecological zones, J. Appl. Rem. Sens.,

1181   14, 022211, https://doi.org/10.1117/1.JRS.14.022211, 2020.

1182 Zhao, J., Yu, L., Liu, H., Huang, H., Wang, J., and Gong, P.: Towards an open and synergistic framework

1183   for mapping global land cover, PeerJ, 9, e11877, https://doi.org/10.7717/peerj.11877, 2021.

1184 Zheng, W., Liu, Y., Yang, X., and Fan, W.: Spatiotemporal variations of forest vegetation phenology and

1185   its response to climate change in northeast China, Remote Sensing, 14, 2909,

1186   https://doi.org/10.3390/rs14122909, 2022.

1187